



# On a simple and effective thermal open boundary condition for convective heat transfer problems

Xiaoyu Liu<sup>a,b</sup>, Zhi Xie<sup>a</sup>, Suchuan Dong<sup>b,\*</sup>

<sup>a</sup> College of Information Science and Engineering, Northeastern University, China

<sup>b</sup> Center for Computational and Applied Mathematics, Department of Mathematics, Purdue University, USA

## ARTICLE INFO

### Article history:

Received 21 October 2019

Revised 8 January 2020

Accepted 9 January 2020

### Keywords:

Thermal open boundary  
Thermal open boundary condition  
Outflow boundary condition  
Open boundary condition  
Heat transfer  
Navier-Stokes equations

## ABSTRACT

We present an effective thermal open boundary condition for convective heat transfer problems on domains involving outflow/open boundaries. This boundary condition is energy-stable, and it ensures that the contribution of the open boundary will not cause an “energy-like” temperature functional to increase over time, irrespective of the state of flow on the open boundary. It is effective in coping with thermal open boundaries even in flow regimes where strong vortices or backflows are prevalent on such boundaries, and it is straightforward to implement. Extensive numerical simulations are presented to demonstrate the stability and effectiveness of our method for heat transfer problems with strong vortices and backflows occurring on the open boundaries. Simulation results are compared with previous works to demonstrate the accuracy of the presented method.

© 2020 Elsevier Ltd. All rights reserved.

## 1. Introduction

In this work we focus on the numerical simulation of convective heat transfer in fluid flows on domains involving outflow/open boundaries. The domain boundary is open in the sense that the fluid and the heat can freely leave or enter the domain through such a boundary. This type of problems are typically encountered in flows with physically unbounded domains, such as wakes, jets, shear layers, and cardiovascular or respiratory networks [25]. Buoyancy-driven flows such as the natural convection in open-ended cavities or open channels are other examples [15,16,21,68], which have widespread applications in solar energy receivers, cooling of electronics, and control of smoke or fire. To numerically simulate such problems, it is necessary to truncate the domain to a finite size, and some outflow/open boundary condition (OBC) will be needed for the artificial boundary. How to properly deal with the open boundary oftentimes holds the key to successful simulations of these problems. This turns out to be a very challenging problem [37,59] as the Reynolds number increases to moderate and high values. A well-known issue, at least for the flow simulations, is the backflow issue and the so-called backflow instability [23,52]. This refers to the difficulty encountered in flow simulations when strong vortices or backflows occur at the outflow/open boundary at moderate and high Reynolds numbers. Many open

boundary conditions that work well at low Reynolds numbers, such as the traction-free condition [4,29,35,38,48,59,63] and the convective condition [32,37,41,53,54,58,62], cease to work and become unstable when strong vortices and backflows are present at the outflow/open boundary. It is observed that an otherwise stable computation can instantly blow up when a strong vortex passes through the outflow/open boundary [23–26,65]. The backflow instability issue has attracted a number of efforts in the past years. A class of methods, the so-called energy-stable open boundary conditions [22,23,25,27,28,52,66], turn out to be particularly effective for overcoming the backflow instability; see also related works in [3,8,10–12,30,33,36,39,45,50,57], among others. These energy-stable open boundary conditions, by design, guarantee that the contributions from the open boundary will not cause the total system energy to increase over time, irrespective of the flow situations occurring at the open boundary (e.g. presence of backflows or strong vortices). Therefore, stable results can be obtained with these methods even when strong vortices or backflows occur on the outflow/open boundary at high Reynolds numbers. More importantly from the practical standpoint, these energy-stable OBCs can be implemented in a straightforward way with the commonly-used semi-implicit splitting type (or fractional-step) schemes for the incompressible Navier-Stokes equations [23,27].

For open-boundary convective heat transfer problems, a survey of literature indicates that how to deal with the thermal open boundary, especially for moderate and high Reynolds numbers where strong vortices or backflows are prevalent at the open

\* Corresponding author.

E-mail address: [sdong@purdue.edu](mailto:sdong@purdue.edu) (S. Dong).

boundary, seems to be much less developed when compared with that for the fluid flows as outlined above. The Sommerfeld radiation (or convective) condition (see e.g. [19,54]) and the Neumann type zero-flux condition (see e.g. [1,5–7,20,67]) are traditional boundary conditions for the temperature applied to the open/outflow boundary. In [14,15] the natural convection in an open cavity has been studied numerically with an extended large computational domain and with a smaller domain consisting of the cavity only. On the extended domain the Neumann type zero-flux condition is imposed for both the velocity and the temperature on the outflow boundary [15]. For the smaller domain, on the open boundary of the cavity the authors distinguish the sections where the flow enters the cavity (inflow) and the sections where the flow leaves the cavity (outflow), and impose a temperature Dirichlet condition on the inflow portion and the Neumann zero-flux condition for the temperature on the outflow portion [14]. Additionally, the authors therein employ a Neumann zero-flux condition for the tangential velocity and the divergence-free condition for the normal velocity component on the open boundary [14]. While the use of extended computational domains pushes the open boundary farther away and can partially alleviate the issue that the true boundary condition is unknown [42], this can be computationally costly because of the increased domain size [21]; see also e.g. [34,64] for investigations of the domain size effect on the computed physical quantities. The boundary condition of [14] and its many variants have been widely adopted in studies of natural convection in subsequent years and have been one of the pre-dominant methods for handling thermal open boundaries where backflows may be present; see e.g. [9,18,21,31,43,44,49,61,68], among others.

In the current paper we present a new thermal open boundary condition that is energy-stable and effective for simulating convective heat transfer problems involving outflow/open boundaries, even at high (or moderate) Reynolds numbers when strong vortices or backflows occur on the open boundary. This boundary condition is formulated such that the contribution of the open/outflow boundary will not cause an “energy-like” temperature function to increase over time, regardless of the state of flow at the open boundary. The form of this thermal open boundary condition has much been inspired by the open boundary conditions from [23] for the incompressible Navier-Stokes equations. In particular, it contains an inertial term (time derivative of temperature) and an extra nonlinear term combining the velocity and the temperature, apart from the temperature directional derivative at the boundary. The nonlinear term in the thermal open boundary condition can be analogized to a term in those open boundary conditions for the incompressible Navier-Stokes equations [11,23,27,52], and it also bears a similarity to the conditions considered in [2,13,51,55,56].

The presented thermal open boundary condition can be implemented in a straightforward fashion. In the current paper we discretize this open boundary condition and the heat transfer equation based on a semi-implicit scheme. Upon discretization, this open boundary condition becomes a Robin-type condition for the temperature, and is implemented using a high-order spectral element technique [40,60,69]. The discretized system of algebraic equations involves a coefficient matrix that is constant and time-independent and can be pre-computed. The current scheme for the thermal open boundary condition, with no change, also applies to finite element-type techniques. We note that the current thermal open boundary condition is much simpler to implement than the commonly-used boundary condition from [14]. The condition of [14] imposes a temperature Dirichlet condition on the backflow region of the boundary. Since such a region is dynamic and changes over time, this in general will require the re-computation and re-factorization (at least partially) of the temperature coefficient matrix every time step in the implementation. For finite element type methods, the dynamic nature of the backflow region on

the open boundary can make the implementation of the temperature Dirichlet condition especially difficult.

We combine the presented thermal open boundary condition, together with the open boundary condition from [23] for the incompressible Navier-Stokes equations, to simulate convective heat transfer on domains involving outflow/open boundaries. Only one-way coupling between the velocity and the temperature (velocity influencing temperature, but not the other way) is considered in the current work. We have performed extensive numerical experiments to test the presented method, especially in regimes of high or fairly high Reynolds numbers, when strong vortices and backflows become prevalent at the open boundary and the backflow instability becomes a severe issue to conventional methods. We compare our simulations with previous works to demonstrate the accuracy of the current method. The long-term stability of this method has been demonstrated in the presence of strong vortices and backflows at the outflow/open boundaries. We show that in such situations the current thermal open boundary condition leads to reasonable simulation results, while the Neumann-type zero-flux condition produces unphysical temperature distributions.

The contributions of this paper lie in the thermal open boundary condition developed herein and the numerical scheme for treating the presented open boundary condition. Particularly noteworthy are the effectiveness of the method in coping with thermal open boundaries where strong vortices or backflows may be present, and its ease in implementation.

The rest of this paper is organized as follows. In Section 2 we present the thermal open boundary condition, look into its energy stability, and develop a semi-implicit scheme for implementing this boundary condition together with the heat transfer equation. In Section 3 we demonstrate the convergence rates, and test the current method using two-dimensional simulations of the heat transfer in two canonical flows: the flow past a circular cylinder and a jet impinging on a wall. Simulations are compared with previous works to show the accuracy of our method. We also demonstrate the method’s long-term stability in regimes where strong vortices and backflows are prevalent at the outflow/open boundaries. Section 4 concludes the presentation with some closing remarks. Appendix A provides a summary of the open boundary condition and the numerical scheme from [23] for the incompressible Navier-Stokes equations, which are employed in the current work. Appendix B and Appendix C provide derivations of two equations and the proof of a theorem in the main text.

## 2. Energy-stable thermal open boundary condition

### 2.1. Heat transfer equation and energy-stable open boundary condition

Consider a domain  $\Omega$  in two or three dimensions, and an incompressible flow contained within. We focus on the heat transfer in this system. The problem is described by the following system of equations (in non-dimensional form):

$$\frac{\partial \mathbf{u}}{\partial t} + \mathbf{u} \cdot \nabla \mathbf{u} + \nabla p - \nu \nabla^2 \mathbf{u} = \mathbf{f}(\mathbf{x}, t), \quad (1a)$$

$$\nabla \cdot \mathbf{u} = 0, \quad (1b)$$

$$\frac{\partial T}{\partial t} + \mathbf{u} \cdot \nabla T = \alpha \nabla^2 T + g(\mathbf{x}, t), \quad (1c)$$

where  $\mathbf{u}(\mathbf{x}, t)$  is the non-dimensional velocity,  $p(\mathbf{x}, t)$  is the non-dimensional pressure,  $T(\mathbf{x}, t)$  is the non-dimensional temperature (possibly with some reference temperature subtracted),  $\mathbf{f}$  is an external body force,  $g(\mathbf{x}, t)$  is an external volumetric heat source term, and  $\mathbf{x}$  denotes the spatial coordinate and  $t$  is time.  $\nu$  is the

inverse of the Reynolds number ( $Re$ ) or non-dimensional viscosity,

$$\nu = \frac{1}{Re} = \frac{\nu_f}{U_0 L} \quad (2)$$

where  $\nu_f$  is the kinematic viscosity of the fluid,  $U_0$  is the velocity scale and  $L$  is the length scale.  $\alpha$  is the inverse of the Peclet number or the non-dimensional thermal diffusivity,

$$\alpha = \frac{1}{Pe} = \frac{\alpha_f}{U_0 L}, \quad (3)$$

where  $\alpha_f$  is the thermal diffusivity of the fluid. We assume that both  $\nu$  and  $\alpha$  are constants. In the current work we will consider only the one-way coupling between the flow and temperature. In other words, the flow influences the temperature distribution, while the effect of the temperature on the flow will not be accounted for. In addition, some other effects such as the heat production due to the viscous dissipation will also be ignored. Note that Eqs. (1a) and (1b) are the incompressible Navier-Stokes equations describing the motion of the fluid.

Let  $\partial\Omega$  denote the boundary of the domain  $\Omega$ . We assume that  $\partial\Omega$  consists of two types (non-overlapping with each other),  $\partial\Omega = \partial\Omega_d \cup \partial\Omega_o$ , with the following properties:

- $\partial\Omega_d$  is the inflow or solid-wall boundary. On  $\partial\Omega_d$  the velocity  $\mathbf{u}$  is known. In terms of the temperature, we assume that  $\partial\Omega_d$  further consists of two sub-types (non-overlapping),  $\partial\Omega_d = \partial\Omega_{dd} \cup \partial\Omega_{dn}$ . On  $\partial\Omega_{dd}$  the temperature is known, and on  $\partial\Omega_{dn}$  the heat flux is known.
- $\partial\Omega_o$  is the outflow/open boundary. On  $\partial\Omega_o$  none of the field variables (velocity, pressure, temperature) is known.

How to deal with the thermal open/outflow boundary  $\partial\Omega_o$  is the subject of the current study. Open boundary conditions for the incompressible Navier-Stokes equations have been studied extensively in a number of previous works (see e.g. [12,23,25,27,37,52,59], among others). In this paper, for the Navier-Stokes equations, we will employ the open boundary condition developed in [23]. This boundary condition, together with a corresponding numerical algorithm, is summarized in the Appendix A for the sake of completeness.

We now concentrate on how to deal with the open/outflow boundary for the heat transfer Eq. (1c). Multiplying Eq. (1c) by  $T$  and integrating over the domain  $\Omega$ , we obtain the following balance equation,

$$\begin{aligned} \frac{\partial}{\partial t} \int_{\Omega} \frac{1}{2} |T|^2 d\Omega &= -\alpha \int_{\Omega} |\nabla T|^2 d\Omega + \int_{\Omega} \mathbf{g}(\mathbf{x}, t) T d\Omega + \int_{\partial\Omega_{dd} \cup \partial\Omega_{dn}} \\ &\left[ \alpha \mathbf{n} \cdot \nabla T - \frac{1}{2} (\mathbf{n} \cdot \mathbf{u}) T \right] T dA \\ &+ \int_{\partial\Omega_o} \underbrace{\left[ \alpha \mathbf{n} \cdot \nabla T - \frac{1}{2} (\mathbf{n} \cdot \mathbf{u}) T \right] T dA}_{\text{outflow boundary term (OBT)}}, \end{aligned} \quad (4)$$

where  $\mathbf{n}$  is the outward-pointing unit vector normal to the boundary, and we have used integration by part, Eq. (1b) and the divergence theorem. The quantity  $\frac{1}{2}|T|^2$  can be considered as an effective “energy” for the heat transfer equation. The last surface integral on the right hand side (RHS) represents the contribution of the open/outflow boundary to this balance equation for the effective energy. This term (OBT) is indefinite, and can be positive or negative depending on the imposed boundary condition and the flow state on  $\partial\Omega_o$ . In particular, with the Neumann-type zero-flux condition (see e.g. [1,20,67]),

$$\mathbf{n} \cdot \nabla T = 0, \quad \text{on } \partial\Omega_o, \quad (5)$$

this open-boundary term would become positive locally when backflow occurs (i.e.  $\mathbf{n} \cdot \mathbf{u} < 0$ ) on the outflow/open boundary,

e.g. when strong vortices pass through  $\partial\Omega_o$  at moderate or high Reynolds numbers. This can cause un-controlled growth in the effective energy, leading to poor simulation results or numerical instabilities.

We are interested in seeking open boundary conditions for the temperature such that the open-boundary term in the balance Eq. (4) is always non-positive, regardless of the state of flow on the open boundary  $\partial\Omega_o$ . As such, the contribution from the outflow/open boundary will not cause the effective energy  $\frac{1}{2}|T|^2$  to grow over time, in the absence of the external heat source and with appropriate boundary conditions for the other types of boundaries. This will be conducive to the stability of computations. We refer to such conditions as energy-stable thermal open boundary conditions.

In the current work, we consider the following open boundary condition for the temperature,

$$\alpha D_0 \frac{\partial T}{\partial t} + \alpha \mathbf{n} \cdot \nabla T - [(\mathbf{n} \cdot \mathbf{u}) T] \Theta_0(\mathbf{n}, \mathbf{u}) = 0, \quad \text{on } \partial\Omega_o. \quad (6)$$

In this equation  $D_0 \geq 0$  is a chosen constant, and  $U_c = \frac{1}{D_0}$  plays the role of a convection velocity scale on the outflow/open boundary  $\partial\Omega_o$ . In practice, one can first estimate the convection velocity scale  $U_c$  on  $\partial\Omega_o$  and then set  $D_0 = \frac{1}{U_c}$  in the boundary condition (6).  $\Theta_0(\mathbf{n}, \mathbf{u})$  is a smoothed step function given by (see [23,27]),

$$\begin{aligned} \Theta_0(\mathbf{n}, \mathbf{u}) &= \frac{1}{2} \left( 1 - \tanh \frac{\mathbf{n} \cdot \mathbf{u}}{U_0 \delta} \right); \\ \lim_{\delta \rightarrow 0} \Theta_0(\mathbf{n}, \mathbf{u}) &= \Theta_{s0}(\mathbf{n}, \mathbf{u}) = \begin{cases} 1, & \text{if } \mathbf{n} \cdot \mathbf{u} < 0, \\ 1/2, & \text{if } \mathbf{n} \cdot \mathbf{u} = 0, \\ 0, & \text{if } \mathbf{n} \cdot \mathbf{u} > 0, \end{cases} \end{aligned} \quad (7)$$

where  $U_0$  is the characteristic velocity scale, and  $\delta > 0$  is a small constant that controls the sharpness of the smoothed step function. The function is sharper with a smaller  $\delta$ . As  $\delta \rightarrow 0$ ,  $\Theta_0(\mathbf{n}, \mathbf{u})$  approaches the step function  $\Theta_{s0}(\mathbf{n}, \mathbf{u})$ , taking the unit value if  $\mathbf{n} \cdot \mathbf{u} < 0$  and vanishing if  $\mathbf{n} \cdot \mathbf{u} > 0$ . Therefore the term involving  $\Theta_0$  in the boundary condition (6) only takes effect in the regions of backflow on the outflow/open boundary  $\partial\Omega_o$ .

The form of this thermal open boundary condition (6) has much been inspired by the boundary condition for the incompressible Navier-Stokes equations from [23]. The boundary condition (6), with  $\delta$  sufficiently small, is an energy-stable open boundary condition for the heat transfer equation. Let us assume for now that there is no heat source (or sink) inside the domain or on the Dirichlet/Neumann boundaries, more specifically,

$$\begin{cases} \mathbf{g}(\mathbf{x}, t) = 0, & \text{on } \Omega; \\ \mathbf{u} = 0, & \text{on } \partial\Omega_d = \partial\Omega_{dd} \cup \partial\Omega_{dn}; \\ T = 0, & \text{on } \partial\Omega_{dd}; \\ \mathbf{n} \cdot \nabla T = 0, & \text{on } \partial\Omega_{dn}. \end{cases} \quad (A1)$$

Then with the boundary condition (6) on  $\partial\Omega_o$ , the balance Eq. (4) is reduced to, under the assumption (A1) and as  $\delta \rightarrow 0$ ,

$$\begin{aligned} \frac{\partial}{\partial t} \left( \int_{\Omega} \frac{1}{2} |T|^2 d\Omega + \alpha D_0 \int_{\partial\Omega_o} \frac{1}{2} |T|^2 dA \right) \\ = -\alpha \int_{\Omega} |\nabla T|^2 d\Omega + \int_{\partial\Omega_o} \frac{1}{2} (\mathbf{n} \cdot \mathbf{u}) T^2 [2\Theta_{s0}(\mathbf{n}, \mathbf{u}) - 1] dA \\ = -\alpha \int_{\Omega} |\nabla T|^2 d\Omega - \int_{\partial\Omega_o} \frac{1}{2} (\mathbf{n} \cdot \mathbf{u}) |T|^2 dA. \end{aligned} \quad (8)$$

The details for the derivation of Eq. (8) are provided in the Appendix B.

The energy balance Eq. (8) implies that the non-negative term  $(\int_{\Omega} \frac{1}{2} |T|^2 d\Omega + \alpha D_0 \int_{\partial\Omega_o} \frac{1}{2} |T|^2 dA)$  will not increase over time. With  $D_0 > 0$ , this equation provides an upper bound for both  $\int_{\Omega} \frac{1}{2} |T|^2 d\Omega$ , which can be considered as some “effective energy”, and the quantity  $\int_{\partial\Omega_o} \frac{1}{2} |T|^2 dA$  on the open boundary. This effectively provides a control over the temperature on the outflow/open boundary. Note that this control results from the inertial term  $\frac{\partial T}{\partial t}$  in the current thermal open boundary condition. Without this

term, e.g. by setting  $D_0 = 0$ , the control over the temperature on the outflow/open boundary will be lost. This feature regarding the temperature provided by the current thermal open boundary condition is analogous to that regarding the velocity observed in [23]. The open boundary condition for the incompressible Navier-Stokes equations from [23], thanks to a velocity inertial term therein, has been observed to provide a control over the velocity on the open boundary [23].

**Remark 2.1.** One can also consider the following more general form of open boundary condition for the temperature,

$$\alpha D_0 \frac{\partial T}{\partial t} + \alpha \mathbf{n} \cdot \nabla T - \left[ \frac{\theta}{2} (\mathbf{n} \cdot \mathbf{u}) T \right] \Theta_0(\mathbf{n}, \mathbf{u}) = 0, \quad \text{on } \partial\Omega_o, \quad (9)$$

where the parameter  $\theta$  is a chosen constant satisfying  $\theta \geq 1$ . The boundary condition (6) corresponds to (9) with  $\theta = 2$ . Analogous to Eq. (8), we can show that Eq. (9), with  $\theta \geq 1$  and  $\delta$  sufficiently small, represents a family of energy-stable thermal open boundary conditions, because in this case Eq. (4) is reduced to, under the assumption (A1) and as  $\delta \rightarrow 0$ ,

$$\begin{aligned} & \frac{\partial}{\partial t} \left( \int_{\Omega} \frac{1}{2} |T|^2 d\Omega + \alpha D_0 \int_{\partial\Omega_o} \frac{1}{2} |T|^2 dA \right) \\ &= -\alpha \int_{\Omega} |\nabla T|^2 d\Omega + \int_{\partial\Omega_o} \frac{1}{2} (\mathbf{n} \cdot \mathbf{u}) T^2 [\theta \Theta_{s0}(\mathbf{n}, \mathbf{u}) - 1] dA \\ &\leq -\alpha \int_{\Omega} |\nabla T|^2 d\Omega. \end{aligned} \quad (10)$$

The details for the derivation of Eq. (10) are provided in the Appendix B. More specifically, we have the following result:

**Theorem 2.1.** Under the assumption (A1), for the open boundary condition (9) with  $\theta > 1$  on  $\partial\Omega_o$ , there exists a  $\delta_0 = \delta_0(\mathbf{u}, T) > 0$  such that for all  $0 < \delta < \delta_0$ ,

$$\frac{\partial}{\partial t} \left( \int_{\Omega} \frac{1}{2} |T|^2 d\Omega + \alpha D_0 \int_{\partial\Omega_o} \frac{1}{2} |T|^2 dA \right) \leq -\alpha \int_{\Omega} |\nabla T|^2 d\Omega.$$

The proof of this theorem is provided in the Appendix C.

Apart from the outflow/open boundary, we impose the following Dirichlet condition for the temperature on  $\partial\Omega_{dd}$ ,

$$T = T_d(\mathbf{x}, t), \quad \text{on } \partial\Omega_{dd}, \quad (11)$$

where  $T_d(\mathbf{x}, t)$  denotes the boundary temperature distribution, and the following Neumann type condition on  $\partial\Omega_{dn}$ ,

$$\mathbf{n} \cdot \nabla T = g_c(\mathbf{x}, t), \quad \text{on } \partial\Omega_{dn}, \quad (12)$$

where  $g_c$  is a prescribed term associated with the boundary heat flux. In addition, we assume the following initial condition for the temperature,

$$T(\mathbf{x}, 0) = T_{in}(\mathbf{x}) \quad (13)$$

where  $T_{in}$  denotes the initial temperature distribution.

Besides the temperature, the incompressible Navier-Stokes Eqs. (1a)–(1b) also require appropriate boundary conditions and initial conditions. The boundary and initial conditions for the Navier-Stokes equations employed in the current work are summarized in the Appendix A.

## 2.2. Numerical algorithm and implementation

Let us now consider how to numerically solve the heat transfer Eq. (1c), together with the open boundary condition (6) (or (9)) for  $\partial\Omega_o$ , and the boundary conditions (11) for  $\partial\Omega_{dd}$  and (12) for  $\partial\Omega_{dn}$ . We assume that the velocity  $\mathbf{u}$  has already been computed by solving the incompressible Navier-Stokes equations (1a)–(1b), together with appropriate boundary conditions for  $\partial\Omega_d$  and  $\partial\Omega_o$ . The numerical algorithm employed in the current work for solving the incompressible Navier-Stokes equations stems from our previous work [23], which has been summarized in Appendix A as mentioned before,

We next focus on the solution of the temperature field. We rewrite the boundary conditions (6) and (9) into a unified form,

$$\alpha D_0 \frac{\partial T}{\partial t} + \alpha \mathbf{n} \cdot \nabla T - H(\mathbf{n}, \mathbf{u}, T) = g_b(\mathbf{x}, t), \quad \text{on } \partial\Omega_o, \quad (14)$$

where

$$H(\mathbf{n}, \mathbf{u}, T) = \begin{cases} [(\mathbf{n} \cdot \mathbf{u}) T] \Theta_0(\mathbf{n}, \mathbf{u}), & \text{for boundary condition (6),} \\ \left[ \frac{\theta}{2} (\mathbf{n} \cdot \mathbf{u}) T \right] \Theta_0(\mathbf{n}, \mathbf{u}), & \text{for general form (9),} \end{cases} \quad (15)$$

and  $g_b$  is a prescribed source term for the purpose of numerical testing only, which will be set to  $g_b = 0$  in actual simulations.

Let  $n \geq 0$  denote the time step index, and  $(\cdot)^n$  denote the variable  $(\cdot)$  at time step  $n$ . Let  $J$  ( $J = 1$  or  $2$ ) denote the temporal order of accuracy. Given  $T^n$  and  $\mathbf{u}^{n+1}$  (computed using the algorithm from Appendix A), we compute  $T^{n+1}$  based on the following scheme:

$$\frac{\gamma_0 T^{n+1} - \hat{T}}{\Delta t} + \mathbf{u}^{n+1} \cdot \nabla T^{*,n+1} = \alpha \nabla^2 T^{n+1} + g^{n+1}; \quad (16a)$$

$$\begin{aligned} \alpha D_0 \frac{\gamma_0 T^{n+1} - \hat{T}}{\Delta t} + \alpha \mathbf{n} \cdot \nabla T^{n+1} - H(\mathbf{n}, \mathbf{u}^{n+1}, T^{*,n+1}) &= g_b^{n+1}, \\ &\text{on } \partial\Omega_o; \end{aligned} \quad (16b)$$

$$T^{n+1} = T_d^{n+1}, \quad \text{on } \partial\Omega_{dd}; \quad (16c)$$

$$\mathbf{n} \cdot \nabla T^{n+1} = g_c^{n+1}, \quad \text{on } \partial\Omega_{dn}. \quad (16d)$$

In the above equations  $\Delta t$  is the time step size.  $\frac{1}{\Delta t} (\gamma_0 T^{n+1} - \hat{T})$  is an approximation of  $\frac{\partial T}{\partial t}|^{n+1}$  based on the  $J$ -th order backward differentiation formula (BDF), in which

$$\gamma_0 = \begin{cases} 1, & J = 1, \\ 3/2, & J = 2; \end{cases} \quad \hat{T} = \begin{cases} T^n, & J = 1, \\ 2T^n - \frac{1}{2}T^{n-1}, & J = 2. \end{cases} \quad (17)$$

$T^{*,n+1}$  is a  $J$ -th order explicit approximation of  $T^{n+1}$ , specifically given by

$$T^{*,n+1} = \begin{cases} T^n, & J = 1, \\ 2T^n - T^{n-1}, & J = 2. \end{cases} \quad (18)$$

Note that  $H(\mathbf{n}, \mathbf{u}^{n+1}, T^{*,n+1})$  is given by Eq. (15).

In the current work we employ  $C^0$ -continuous high-order spectral elements [40,69] for spatial discretizations. Let  $\varphi(\mathbf{x})$  denote an arbitrary test function that vanishes on  $\partial\Omega_{dd}$ , i.e.  $\varphi|_{\partial\Omega_{dd}} = 0$ . Multiplying  $\varphi$  to Eq. (16a) and integrating over the domain  $\Omega$ , we obtain the weak form about  $T^{n+1}$ ,

$$\begin{aligned} & \int_{\Omega} \nabla T^{n+1} \cdot \nabla \varphi d\Omega + \frac{\gamma_0}{\alpha \Delta t} \int_{\Omega} T^{n+1} \varphi d\Omega + \frac{\gamma_0 D_0}{\Delta t} \int_{\partial\Omega_o} T^{n+1} \varphi dA \\ &= \frac{1}{\alpha} \int_{\Omega} \left( g^{n+1} + \frac{\hat{T}}{\Delta t} - \mathbf{u}^{n+1} \cdot \nabla T^{*,n+1} \right) \varphi d\Omega + \int_{\partial\Omega_{dn}} g_c^{n+1} \varphi dA \\ &+ \int_{\partial\Omega_o} \left[ \frac{D_0}{\Delta t} \hat{T} + \frac{1}{\alpha} g_b^{n+1} + \frac{1}{\alpha} H(\mathbf{n}, \mathbf{u}^{n+1}, T^{*,n+1}) \right] \varphi dA, \\ & \quad \forall \varphi \text{ with } \varphi|_{\partial\Omega_{dd}} = 0, \end{aligned} \quad (19)$$

where we have used integration by part, the divergence theorem, and the Eqs. (16b) and (16d).

The weak form (19), together with the Dirichlet condition (16c), can be discretized using  $C^0$  spectral elements in the standard way [40]. Within a time step we first compute the velocity  $\mathbf{u}^{n+1}$  and pressure  $p^{n+1}$  using the algorithm from the Appendix A, and then solve Eq. (19) together with (16c) for the temperature  $T^{n+1}$ .

**Remark 2.2.** When  $D_0 = 0$ , the boundary conditions (6) and (9) are reduced to

$$\alpha \mathbf{n} \cdot \nabla T - [(\mathbf{n} \cdot \mathbf{u})T] \Theta_0(\mathbf{n}, \mathbf{u}) = 0, \quad \text{on } \partial\Omega_o; \quad (20)$$

$$\alpha \mathbf{n} \cdot \nabla T - \left[ \frac{\theta}{2} (\mathbf{n} \cdot \mathbf{u})T \right] \Theta_0(\mathbf{n}, \mathbf{u}) = 0, \quad \text{on } \partial\Omega_o. \quad (21)$$

The scheme given in (16a)–(16d) equally applies to these two forms of boundary conditions, by simply setting  $D_0 = 0$  and  $\mathbf{g}_b = 0$  within. In this case, the weak form is still given by (19), with  $D_0 = 0$  and  $\mathbf{g}_b = 0$ .

It is noted that in [13] the authors therein use an effective temperature in the formulation of the open boundary condition. They define the effective temperature as the convex average of the outlet temperature and the external temperature, and refer to the average coefficient, which can depend on the velocity, as the function  $\beta$ . In [13]  $\beta$  is defined to be a continuous (may be discontinuous at the origin) function taking values between 0 and 1. We would like to mention that Eq. (20) is similar in form to the boundary condition considered in [13] (with a particular choice for the  $\beta$  function and assumption about the external temperature). Eq. (21), with  $1 \leq \theta \leq 2$ , can also be represented using some particular forms for the  $\beta$  function. We further note that the conditions represented by Eq. (21), with  $\theta > 2$ , cannot be represented by the  $\beta$  function defined therein, because these conditions take values beyond the range [0,1]. Therefore, they do not correspond to the conditions considered in [13]. We would also like to mention that the forms of the temperature boundary conditions represented by Eqs. (20) and (21) are analogous to those forms of velocity open boundary conditions that are studied in [27].

### 3. Representative simulations

We next test the performance of the method presented in the previous section using several two-dimensional convective heat transfer problems involving outflow/open boundaries. In particular, we study flow regimes where strong vortices or backflows are prevalent at the outflow/open boundary. In such cases, how to handle the open boundary is the key to successful simulations of these problems. We show that the current method produces stable and reasonable results for the temperature field, while the Neumann type zero-flux condition leads to unphysical temperature distributions on the outflow/open boundary when the vortices pass through.

#### 3.1. Convergence rates

We first demonstrate the spatial and temporal convergence rates of the method from Section 2 by using a manufactured analytic solution to the heat transfer equation. Consider the rectangular domain  $\overline{ABCD}$  shown in Fig. 1(a),  $0 \leq x \leq 2$  and  $-1 \leq y \leq 1$ , and the flow and heat transfer problem on this domain. We employ the following expressions for the flow/temperature fields of a manufactured solution to the governing Eqs. (1a)–(1c),

$$\begin{cases} u = 2 \sin(\pi x) \cos(\pi y) \sin(2t), \\ v = -2 \cos(\pi x) \sin(\pi y) \sin(2t), \\ p = 2 \sin(\pi x) \sin(\pi y) \cos(2t), \\ T = 2 \cos(\pi x) \sin(\pi y) \sin(2t), \end{cases} \quad (22)$$

where  $\mathbf{u} = (u, v)$ . In Eqs. (1a) and (1c) the external force  $\mathbf{f}$  and the source term  $g$  are chosen such that the expressions from (22) satisfy these equations. Note that the  $(u, v)$  expressions in (22) also satisfy the Eq. (1b).

We discretize the domain  $\overline{ABCD}$  using two quadrilateral elements of the same size; see Fig. 1(a). On the sides  $\overline{AD}$ ,  $\overline{AB}$  and

$\overline{BF}$  we impose the Dirichlet condition (11) for the temperature and the Dirichlet condition (25) (in Appendix A) for the velocity, where the boundary temperature and velocity are chosen according to the analytical expressions from (22). The sides  $\overline{FC}$  and  $\overline{CD}$  are assumed to be open boundaries, and we impose the boundary condition (14) for the temperature and the condition (26) for the velocity. In Eq. (14),  $H(\mathbf{n}, \mathbf{u}, T)$  is taken to be the first expression from Eq. (15), and  $\mathbf{g}_b$  is chosen such that the analytical expressions from (22) satisfy the Eq. (14) on the open boundary. In Eq. (26),  $\mathbf{E}(\mathbf{n}, \mathbf{u})$  is given by (27), and  $\mathbf{f}_b$  is chosen such that the analytic expressions of (22) satisfy the Eq. (26) on the open boundary. The initial conditions for the temperature and velocity are given by (13) and (29), respectively, in which  $T_{in}$  and  $\mathbf{u}_{in}$  are chosen according to the analytic expressions from (22) by setting  $t = 0$ .

The scheme from Section 2 is employed to solve for the temperature field, and the algorithm from the Appendix A is employed to solve for the velocity field, in time from  $t = 0$  to  $t_f$  (to be specified below). Then the numerical solution of the temperature at  $t = t_f$  is compared with the analytic expression from (22), and the errors in the  $L^\infty$ ,  $L^2$  and  $H^1$  norms are computed and monitored. In the numerical tests below we employ a fixed non-dimensional viscosity  $\nu = 0.01$  and thermal diffusivity  $\alpha = 0.01$ . Other parameter values include  $D_0 = 1.0$ ,  $U_0 = 1.0$  and  $\delta = 0.05$  in Eqs. (14), (26) and (7). The element order and the time step size are varied respectively in the spatial and temporal convergence tests to study their effects on the numerical errors.

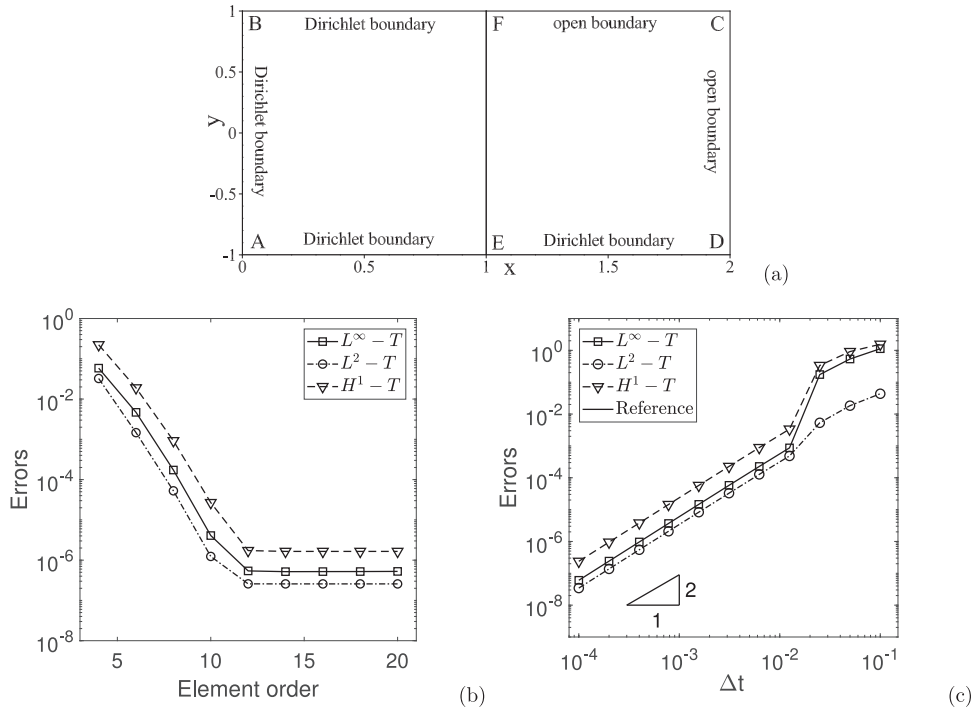
Fig. 1 (b) illustrates the behavior of the method in spatial convergence tests. In this group of tests we employ a fixed  $t_f = 0.1$  and  $\Delta t = 0.001$ , and vary the element order systematically between 4 and 20. The figure shows the  $L^\infty$ ,  $L^2$  and  $H^1$  errors of the temperature at  $t = t_f$  as a function of the element order. For element orders below 12 the errors decrease exponentially with increasing element order. For element orders above 12 the numerical errors are observed to remain at a constant level, due to the saturation of the temporal truncation error.

Fig. 1 (c) illustrates the temporal convergence behavior of the method. In this group of tests a fixed  $t_f = 0.5$  and an element order 16 are employed, and the time step size  $\Delta t$  is varied systematically between  $\Delta t = 0.1$  and  $\Delta t = 1e - 4$ . The figure shows the numerical errors of the temperature as a function of  $\Delta t$  from these tests. It is evident that the method exhibits a temporal second-order convergence rate for the temperature as  $\Delta t$  becomes small.

#### 3.2. Flow past a warm circular cylinder

In this section we use a canonical problem, the heat transfer in the flow past a circular cylinder, to test the performance of the thermal open boundary condition and the numerical scheme herein.

Consider the flow domain shown in Fig. 2, occupying the region  $-2.5d \leq x \leq 6.5d$  and  $-1.5d \leq y \leq 1.5d$ , where  $d = 1$  is the cylinder diameter. The cylinder center coincides with the origin of the coordinate system. A cooler fluid with temperature  $T_0 = 20$  degrees Celsius enters the domain from the left with a uniform velocity  $U_0 = 1$  along the  $x$  direction. The flow exits the domain from the right side. The surface of the cylinder is maintained at a higher temperature  $T_h = 80$  degrees Celsius. The top and bottom sides of the domain ( $y = \pm 1.5d$ ) are assumed to be periodic. This configuration mimics the flow past an infinite array of circular cylinders in the  $y$  direction. We would like to study the heat transfer in this flow. We are particularly interested in the regimes of moderate to fairly high Reynolds numbers, when the vortices generated at the cylinder can persist in the entire wake region and exit the domain on the right. How the current thermal open boundary condition perform in such situations will be studied.



**Fig. 1.** Convergence tests: (a) Flow domain and configuration. (b) Temperature errors ( $L^\infty$ ,  $L^2$  and  $H^1$  norms) as a function of the element order (fixed  $t_f = 0.1$  and  $\Delta t = 0.001$ ). (c) Temperature errors as a function of  $\Delta t$  (fixed  $t_f = 0.5$  and element order 16).

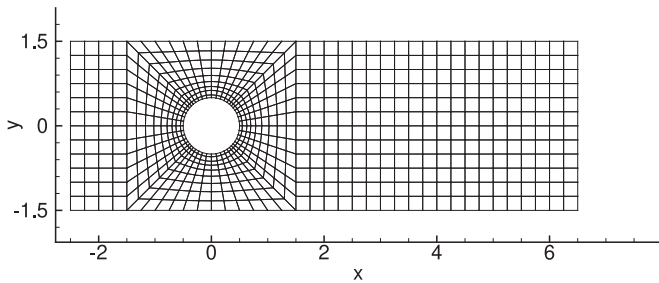


**Fig. 2.** Cylinder flow: Flow domain and the mesh of 720 quadrilateral elements.

We choose the inflow velocity  $U_0$  as the velocity scale, the cylinder diameter  $d$  as the length scale, and the unit temperature  $T_d = 1$  degree Celsius as the temperature scale. Then all the physical variables and parameters are normalized accordingly. So the Reynolds number and the Peclet number are defined in terms of the cylinder diameter in this problem.

We discretize the domain using a mesh of 720 quadrilateral elements; see Fig. 2. On the left boundary ( $x = -2.5d$ ), Dirichlet boundary conditions (11) and (25) are imposed for the temperature and the velocity, respectively, in which the boundary temperature ( $T_d$ ) and velocity ( $\mathbf{w}$ ) are set to the inflow temperature and inflow velocity as given above. On the cylinder surface, no-slip condition is imposed for the velocity, and the Dirichlet condition (11) with  $T_d = T_h = 80$  is imposed for the temperature. Periodic conditions are imposed on the top/bottom boundaries for all field variables. On the right boundary, the open boundary condition (6) is imposed for the temperature, in which we set  $D_0 = \frac{1}{U_0} = 1$  and  $\delta = 0.05$  for this problem. For the Navier-Stokes equations we impose the open boundary condition (26), with  $\mathbf{f}_b = 0$  and  $\mathbf{E}(\mathbf{n}, \mathbf{u})$  given by (27).

We employ the algorithm from Section 2 to solve the temperature Eq. (1c) with  $g = 0$  and the algorithm from the Appendix A to solve the Navier-Stokes Eqs. (1a)–(1b) with  $\mathbf{f} = 0$ . We have conducted simulations at three Reynolds numbers ( $Re = 300, 2000$

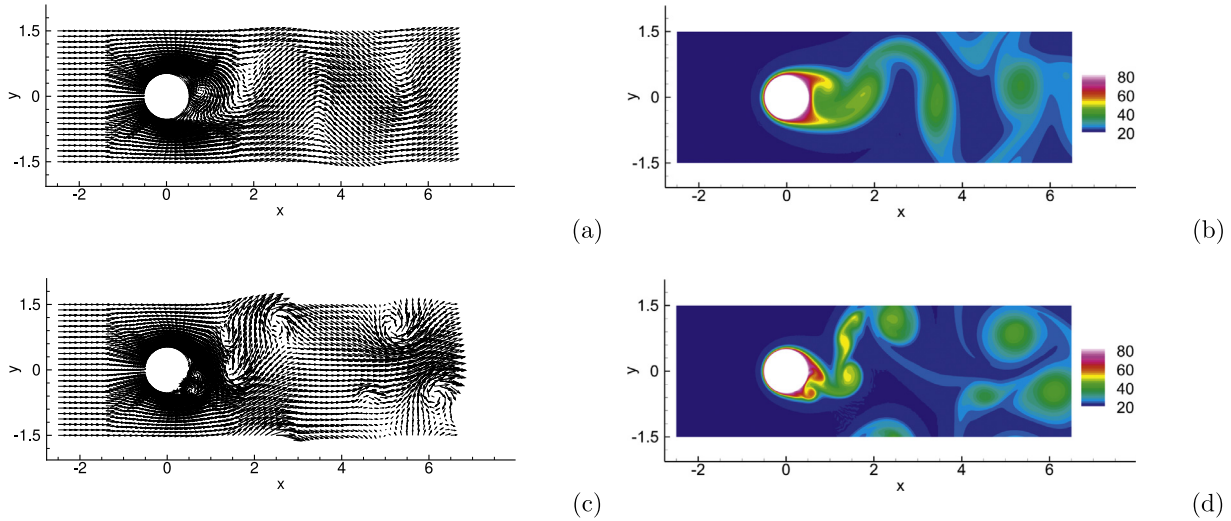
and 5000) and two Peclet numbers (corresponding to  $\alpha = 0.01$  and 0.005). The element order, the time step size, and other simulation parameters are varied in the simulations to study their effects on the results. For any given set of parameter values we have performed long-time simulations so that the flow has reached a statistically stationary state. Therefore, the initial conditions have no effect on the reported results.

Fig. 3 provides an overview of the characteristics of the flow and temperature fields for this problem. It shows the distributions of the instantaneous velocity (left column) and temperature (right column) at Reynolds numbers  $Re = 300$  (top row) and  $Re = 5000$  (bottom row). For  $Re = 300$  (Figs. 3(a) and (b)), the non-dimensional thermal diffusivity is  $\alpha = 0.01$ , and the simulations are performed using an element order 6 and a time step size  $\Delta t = 0.001$ . For  $Re = 5000$  (Figs. 3(c) and (d)), the non-dimensional thermal diffusivity is  $\alpha = 0.005$ , and the results are computed using an element order 8 and a time step size  $\Delta t = 2.5e - 4$ . The flow is unsteady at these Reynolds numbers and is characterized by regular or irregular vortex shedding in the cylinder wake. At the lower  $Re = 300$ , the vortices are quite weak, and no backflow is observed at the outflow boundary (Fig. 3(a)). At the higher Reynolds number  $Re = 5000$ , the vortices persist in the entire wake region, and strong backflows are observed at the outflow boundary while these vortices are passing through. Because the vortices are generated at the cylinder and shed into the wake, the vortex cores contain warmer fluids, as is evident from the temperature distributions in Figs. 3(b) and (d).

To characterize the overall evolution of the temperature field, we have computed and monitored the following quantities:

$$T_{L_2}(t) = \sqrt{\frac{1}{V_\Omega} \int_\Omega [T(\mathbf{x}, t)]^2 d\Omega},$$

$$T_{H_1}(t) = \sqrt{\frac{1}{V_\Omega} \int_\Omega [(T(\mathbf{x}, t))^2 + |\nabla T|^2] d\Omega}, \quad (23)$$



**Fig. 3.** Cylinder flow: Instantaneous velocity distributions (plots (a) and (c)) and temperature distributions (plots (b) and (d)). Plots (a) and (b) are for  $Re = 300$  and  $\alpha = 0.01$ , and plots (c) and (d) are for  $Re = 5000$  and  $\alpha = 0.005$ . Velocity vectors are shown on a sparser set of mesh points for clarity.

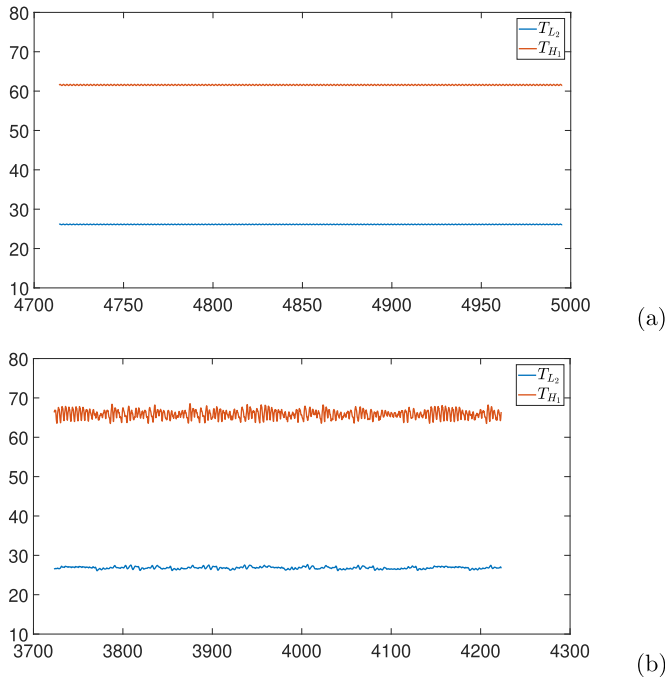


**Fig. 4.** Cylinder flow: Time histories of the  $T_{L_2}(t)$  and  $T_{H_1}(t)$  at Reynolds numbers (a)  $Re = 300$  and (b)  $Re = 2000$ . Thermal diffusivity is  $\alpha = 0.01$  for both cases.

where  $V_\Omega = \int_\Omega d\Omega$  is the volume of the domain. These are basically the  $L^2$  and  $H^1$  norms of the temperature field. Fig. 4 shows time histories of  $T_{L_2}(t)$  and  $T_{H_1}(t)$  at two Reynolds numbers  $Re = 300$  and  $Re = 2000$ . The non-dimensional thermal diffusivity is  $\alpha = 0.01$  for both cases. The results for  $Re = 300$  (Fig. 4(a)) are computed with an element order 5, and those for  $Re = 2000$  (Fig. 4(b)) are obtained with an element order 7. At  $Re = 300$ , both temperature norms exhibit a regular fluctuation in time with a small amplitude. At the higher Reynolds number  $Re = 2000$ , the fluctuations in these temperature signals are much stronger and irregular, especially with  $T_{H_1}(t)$ . The long histories in these plots signify the stability of our simulations. The constant mean level and the invariant characteristics of the fluctuations suggest that the temperature field has reached a statistically stationary state.

**Table 1**

Cylinder flow: Time-averaged mean and root-mean-square (rms) of  $T_{L_2}(t)$  and  $T_{H_1}(t)$  computed using various element orders at two Reynolds numbers. Thermal diffusivity is  $\alpha = 0.01$ .

Reynolds number	Element order	$\bar{T}_{L_2}$	$T'_{L_2}$	$\bar{T}_{H_1}$	$T'_{H_1}$
300	3	26.124	5.27e-2	61.563	0.104
	4	26.128	5.33e-2	61.563	0.103
	5	26.130	5.37e-2	61.566	0.104
	6	26.129	5.36e-2	61.564	0.104
2000	5	26.786	0.286	65.895	1.014
	6	26.764	0.314	65.833	0.908
	7	26.825	0.283	65.908	1.016
	8	26.854	0.284	65.932	1.046
	9	26.836	0.280	65.935	1.037

From the time histories of  $T_{L_2}(t)$  and  $T_{H_1}(t)$  we can compute the time-averaged mean and root-mean-square (rms) of these temperatures, which can be compared quantitatively to assess the effect of the simulation parameters. Table 1 lists the mean ( $\bar{T}_{L_2}$  and  $\bar{T}_{H_1}$ ) and rms ( $T'_{L_2}$  and  $T'_{H_1}$ ) values of  $T_{L_2}(t)$  and  $T_{H_1}(t)$  corresponding to a range of element orders, for Reynolds numbers  $Re = 300$  and  $Re = 2000$  with a thermal diffusivity  $\alpha = 0.01$ . We have employed a time step size  $\Delta t = 0.001$  for  $Re = 300$  and  $\Delta t = 5e - 4$  for  $Re = 2000$  in this set of simulations. We observe that, for both Reynolds numbers, the change in the mean and rms temperatures is not significant with increasing element order, indicating a convergence of simulation results with respect to the mesh resolution. In the results reported below, the majority of simulations are performed with an element order 5 for  $Re = 300$  and with an element order 7 for higher Reynolds numbers.

Let us next look into the effect of the open boundary condition on the simulated flow and temperature fields. We observe that for this problem the boundary condition imposed on the outflow boundary, especially at fairly high Reynolds numbers where strong vortices or backflows occur on such boundary, is critical to the stability of computations and to the physical soundness of the simulated temperature field. When the Reynolds number is low (e.g.  $Re = 300$ ), no vortex or backflow occurs at the outflow boundary, and usual open boundary conditions (e.g. the Neumann type zero-flux condition (5)) can work well and produce reasonable results. When the Reynolds number becomes fairly high, e.g. with  $Re \approx 2000$  or larger for the circular cylinder flow, strong vortices or backflows can occur on the open boundary. In such

cases the adoption of the energy-stable open boundary condition developed herein for the temperature field and those from e.g. [23] (see also Appendix A) for the Navier-Stokes equations are critical to the successful simulations of this problem.

These points are demonstrated by two temporal sequences of the velocity and temperature distributions shown in Figs. 5–8. These results correspond to the Reynolds number  $Re = 2000$  and a non-dimensional thermal diffusivity  $\alpha = 0.01$ , and they are obtained respectively using the current thermal open boundary condition (6) and the Neumann-type zero-flux condition (5) for the outflow boundary. Note that in both cases we have employed the open boundary condition (26) with  $\mathbf{E}(\mathbf{n}, \mathbf{u})$  given in (27) for the Navier-Stokes equations. Figs. 5 and 7 show the two separate sequences of velocity fields. Fig. 6 shows the temporal sequence of snapshots of the temperature fields, corresponding to the velocity distributions in Fig. 5, computed using the current thermal open boundary condition (6). Fig. 8 shows the temporal sequence of snapshots of the temperature fields, corresponding to the velocity distributions in Fig. 7, computed using the Neumann-type zero-flux condition (5) for the temperature on the outflow boundary. In these simulations we have employed an element order 8 and a time step size  $\Delta t = 5e - 4$ . At this Reynolds number, strong vortices and backflows can be clearly observed on the outflow boundary (Figs. 5 and 7). The use of the energy-stable OBC from [23] (see Appendix A) for the Navier-Stokes equations employed here is crucial for the stable flow simulation. What is striking concerns the temperature distribution near the outflow boundary obtained by these two methods. A comparison between Figs. 6 and 8 shows that the current thermal OBC (6) and the Neumann-type OBC (5) lead to quite different results near the outflow boundary when the vortices are passing through, and that in such cases the Neumann-type thermal OBC produces apparently unphysical temperature distributions. With the Neumann-type OBC (5), we observe that when a vortex crosses the outflow boundary the computed temperature at the vortex core can attain unphysical values. In Fig. 8 those regions with unphysical temperature distributions are marked by the dashed boxes. The computed temperature in those regions can become nearly zero degrees Celsius (see the dark blue region in the inset of Fig. 8(e)), which is clearly unphysical given the inflow and the cylinder temperature (20 and 80 degrees Celsius, respectively). We observe that the unphysical temperature arises only when the vortices are passing through the outflow boundary, where backflows occur. After the vortices exit the domain, the temperature field near the outflow boundary computed by the Neumann-type OBC (5) is restored to a reasonable distribution. In contrast, with the current thermal OBC (6), we observe that the computed temperature field at/near the outflow boundary exhibits a reasonable distribution throughout the time, particularly when strong vortices pass through the outflow boundary and when backflows occur there. This is evident from Fig. 6.

The above observations are not limited to the Reynolds number  $Re = 2000$ , or thermal diffusivity  $\alpha = 0.01$  (we have also tested  $\alpha = 0.005$ ). At higher Reynolds numbers (we have tested  $Re = 5000$ ,  $\alpha = 0.01$  and  $0.005$ ), the same characteristics in the computed temperature distributions have been observed with regard to the current thermal OBC and the Neumann-type OBC. These results demonstrate a clear advantage of the current thermal OBC for dealing with thermal open boundaries at high (and moderate) Reynolds numbers, when strong vortices or backflows might occur there. At low Reynolds numbers (we have tested  $Re = 300$ ), when no vortices or backflows occur at the outflow boundary, we observe that both the current thermal OBC and the Neumann-type zero-flux OBC produce reasonable temperature distributions for this problem.

### 3.3. Warm jet impinging on a cool wall

In this subsection we test the presented method by simulating the heat transfer in another canonical flow, a jet impinging on a solid wall. At moderate and fairly high Reynolds numbers, the physical instability of the jet and the vortices formed along the jet profile, together with the open domain boundary, pose a significant challenge to the flow and temperature simulations.

We consider the domain depicted in Fig. 9,  $-5d \leq x \leq 5d$  and  $0 \leq y \leq 5d$ , where  $d = 1$  is the jet inlet diameter. The top and bottom of the domain are solid walls, which are maintained at a constant temperature  $T_w = 20$  degrees Celsius. The left and right sides of the domain are open, where the fluid can freely leave or enter the domain. The initial fluid temperature in the domain is assumed to be  $T_{in} = 20$  degrees Celsius, and the fluid is initially assumed to be at rest. In the middle of the top wall there is an orifice with a diameter  $d$ , through which a jet of fluid is issued into the domain. The jet velocity and temperature at the inlet is assumed to have the following distribution:

$$\begin{cases} u = 0, \\ v = -U_0 \left[ (\mathcal{H}(x, 0) - \mathcal{H}(x, R_0)) \tanh \frac{1-x/R_0}{\sqrt{2}\epsilon} \right. \\ \quad \left. + (\mathcal{H}(x, -R_0) - \mathcal{H}(x, 0)) \tanh \frac{1+x/R_0}{\sqrt{2}\epsilon} \right] \\ T = T_w + (T_h - T_w) \left( 1 - \frac{x^2}{R_0^2} \right), \end{cases} \quad (24)$$

where  $R_0 = d/2$  is the jet radius,  $U_0 = 1$  is the velocity scale,  $\epsilon = \frac{1}{40}$ , and  $T_h = 80$  degrees Celsius is the centerline temperature.  $\mathcal{H}(x, a)$  is the Heaviside step function, taking a unit value if  $x \geq a$  and vanishing otherwise. With the above expressions, the inlet velocity has a “top-hat” profile, essentially  $U_0$  except in a thin layer (thickness controlled by the parameter  $\epsilon$ ) near the wall. With this configuration, the jet enters the domain through the inlet, impinges on the bottom wall, and then exits the domain through the open boundaries on the left and right sides. We would like to study the heat transfer in this flow using the method from Section 2.

We use  $U_0$  as the velocity scale,  $d$  as the length scale, and  $T_d = 1$  degree Celsius as the temperature scale. All the physical variables and parameters are then normalized accordingly. So the Reynolds number is defined based on the jet inlet diameter for this problem.

We employ the method presented in Section 2 to solve the heat transfer Eq. (1c) with  $g = 0$ , and the algorithm from the Appendix A to solve the Navier-Stokes Eqs. (1a)–(1b) with  $\mathbf{f} = 0$ . The domain is discretized using a mesh of 800 uniform quadrilateral elements, with 40 elements along the  $x$  direction and 20 elements along the  $y$  direction. On the top and bottom walls, no-slip condition (zero velocity) has been imposed for the velocity, and the Dirichlet condition (11) with  $T_d = T_w = 20$  has been imposed for the temperature. At the jet inlet, we impose the Dirichlet conditions (25) for the velocity and (11) for the temperature, with the boundary velocity and temperature chosen according to the expressions given in (24). On the left/right boundaries of the domain, we impose the open boundary condition (6) for the temperature, with  $D_0 = \frac{1}{U_0}$  and  $\delta = \frac{1}{20}$ , and the condition (26) for the velocity, with  $\mathbf{f}_b = 0$  and  $\mathbf{E}(\mathbf{n}, \mathbf{u})$  given by (27) (for  $Re = 300$  and  $2000$ ) or (28) with  $(\beta_0, \beta_1, \beta_2) = (0, 1, 0)$  (for  $Re = 5000$ ). The initial temperature is set to  $T_{in} = 20$  and the initial velocity is set to zero. We have performed long-time simulations, and the flow and temperature have reached a statistically stationary state. So these initial conditions have no effect on the results reported below. The element order and the time step size are varied systematically in the simulations to study their effects on the simulation results. The problem corresponding to three Reynolds numbers ( $Re=300, 2000$  and  $5000$ )

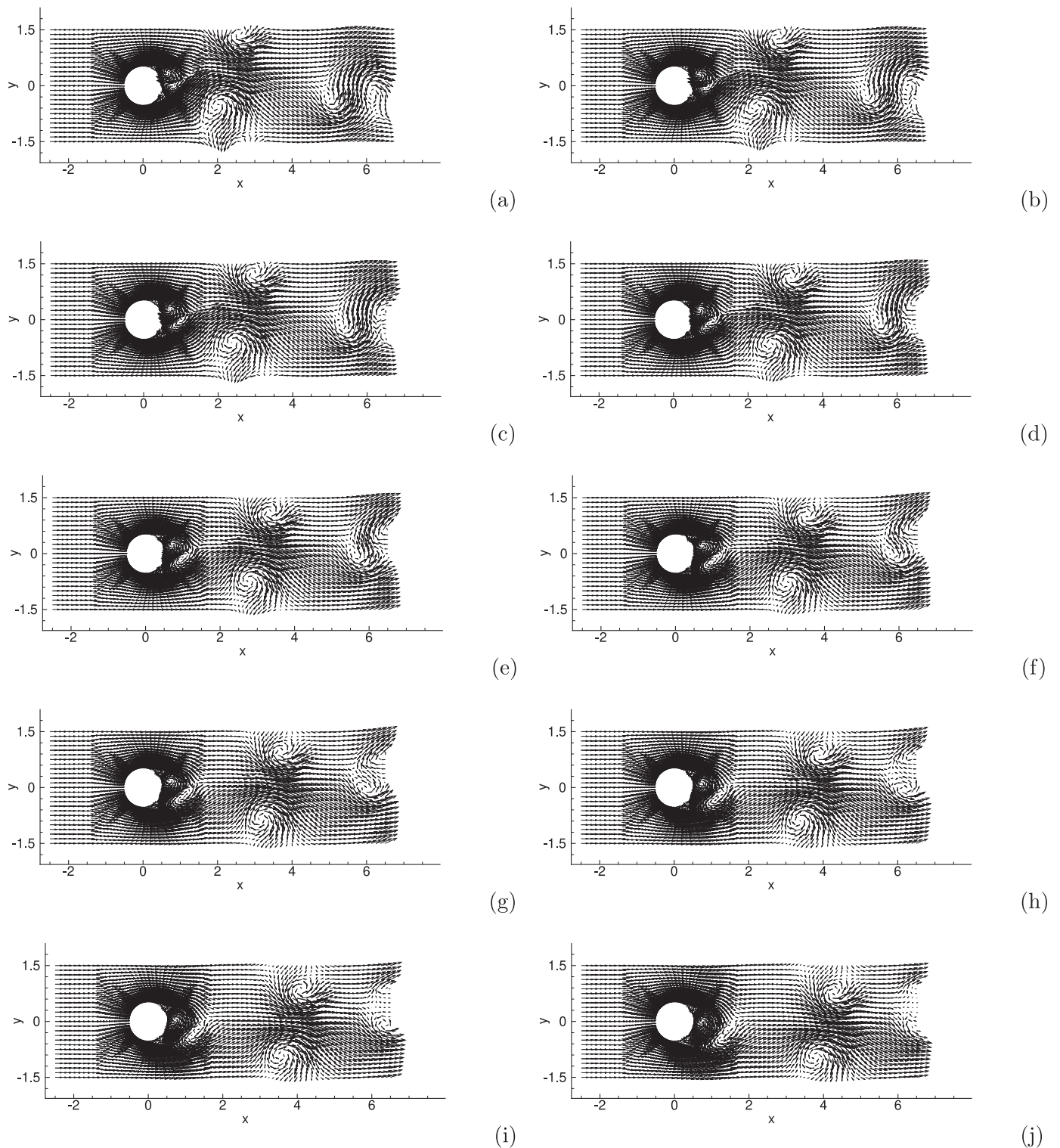


**Fig. 5.** Cylinder flow ( $Re=2000$ ): temporal sequence of snapshots of the velocity distribution, (a)  $t = t_0$ , (b)  $t = t_0 + 0.2$ , (c)  $t = t_0 + 0.4$ , (d)  $t = t_0 + 0.6$ , (e)  $t = t_0 + 0.8$ , (f)  $t = t_0 + 1.0$ , (g)  $t = t_0 + 1.2$ , (h)  $t = t_0 + 1.4$ , (i)  $t = t_0 + 1.6$ , (j)  $t = t_0 + 1.8$ .  $t_0$  is the initial time instant of this sequence. Velocity vectors are plotted on a set of sparser mesh points for clarity.

and two thermal diffusivities ( $\alpha = 0.01$  and  $0.005$ ) has been simulated.

Fig. 10 provides an overview of the distribution characteristics of the velocity and temperature fields obtained using the current method at two Reynolds numbers  $Re = 300$  and  $Re = 2000$  and a non-dimensional thermal diffusivity  $\alpha = 0.01$ . At low Reynolds

numbers (e.g.  $Re = 300$ ) this is a steady flow. The vertical jet splits into two horizontal streams after impinging on the bottom wall, which exit the domain through the open boundaries on the left/right sides. Strong flows are largely confined to regions of the vertical jet and the near-wall horizontal streams (Fig. 10(a)), and the velocity field is quite weak outside these regions. Correspond-

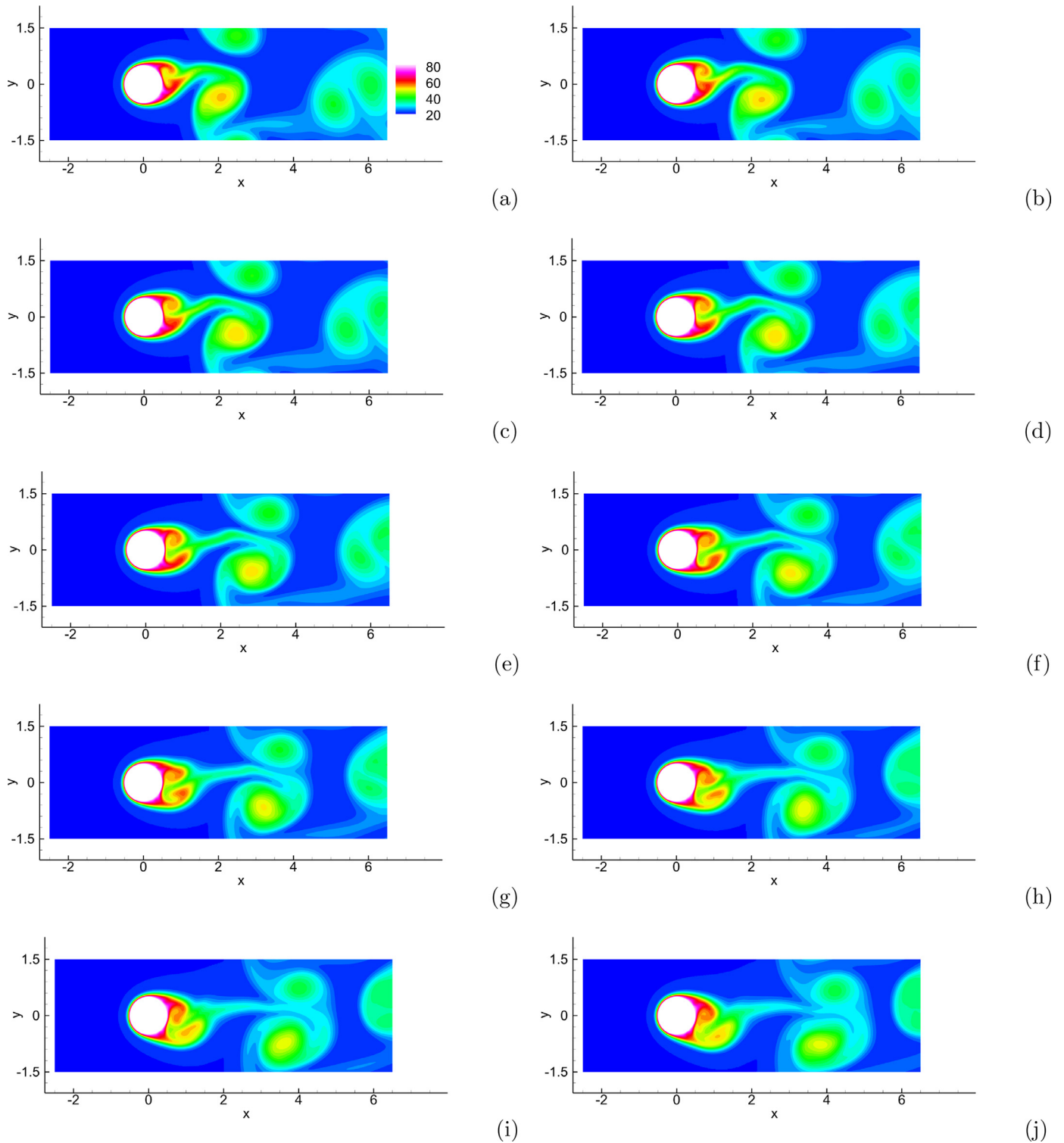


**Fig. 6.** Cylinder flow ( $Re=2000$ ): temporal sequence of snapshots of the temperature distribution computed using the current thermal OBC, at identical time instants as in Fig. 5. (a)  $t = t_0$ . (b)  $t = t_0 + 0.2$ . (c)  $t = t_0 + 0.4$ . (d)  $t = t_0 + 0.6$ . (e)  $t = t_0 + 0.8$ . (f)  $t = t_0 + 1.0$ . (g)  $t = t_0 + 1.2$ . (h)  $t = t_0 + 1.4$ . (i)  $t = t_0 + 1.6$ . (j)  $t = t_0 + 1.8$ . Thermal diffusivity is  $\alpha = 0.01$ .

ingly, warm fluids are confined to the regions of the vertical jet and the horizontal streams, and the temperature decays along the profile of the jet streams (Fig. 10(b)). As the Reynolds number increases (e.g.  $Re = 2000$ ), the vertical jet becomes unstable downstream of the inlet due to the Kelvin-Helmholtz instability, and vortices can be observed to form on both sides of the jet profile

(Fig. 10(c)). These vortices are advected along the vertical and horizontal jet streams and exit the domain through the left/right open boundaries. The temperature distributions at these Reynolds numbers are unsteady and exhibit more complicated features. The vortices are observed to carry warm fluids with them, forming hot spots along the jet profile (Fig. 10(d)).

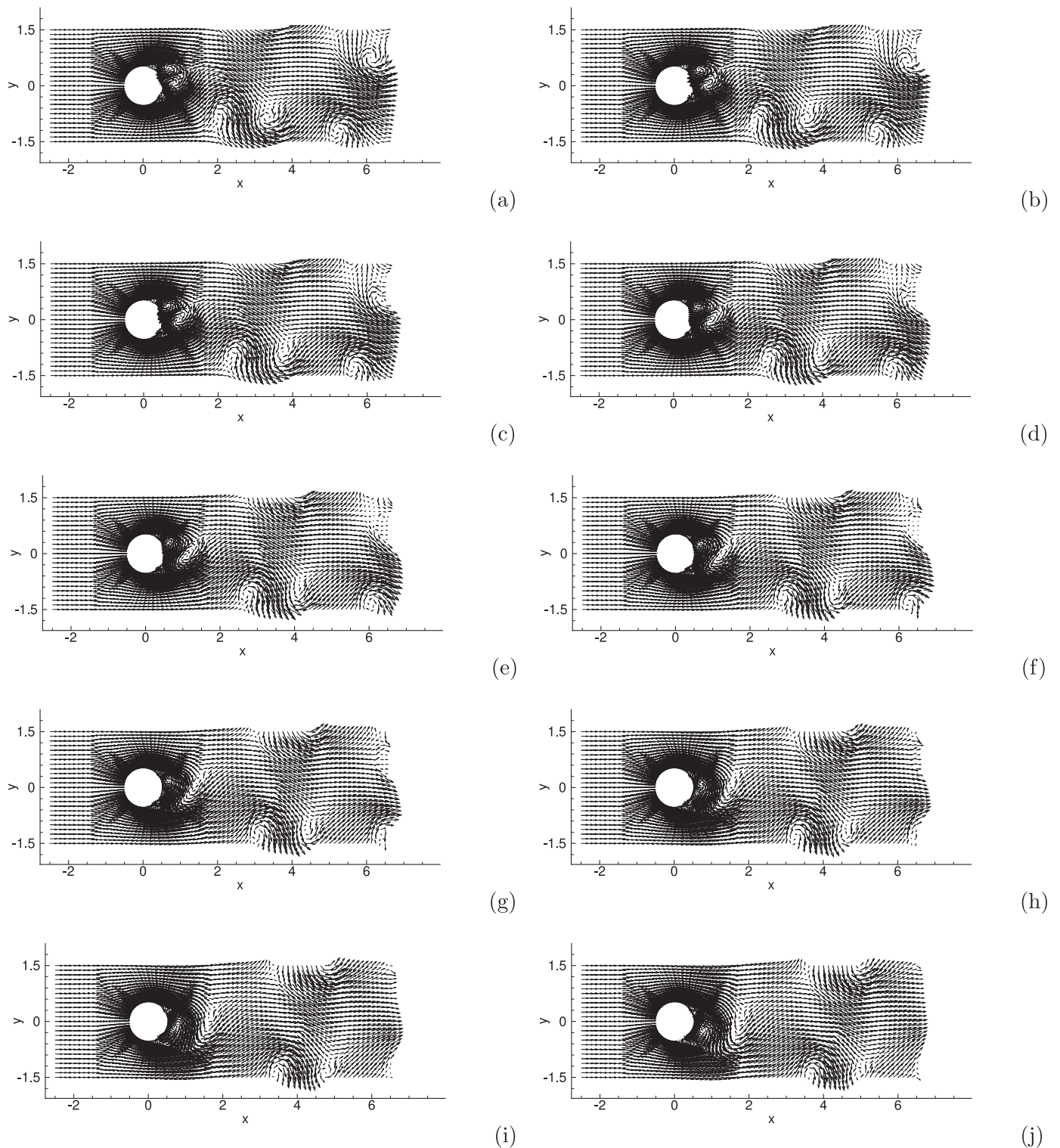


**Fig. 7.** Cylinder flow ( $Re=2000$ ): another temporal sequence of snapshots of the velocity distribution. (a)  $t = t_1$ , (b)  $t = t_1 + 0.2$ , (c)  $t = t_1 + 0.4$ , (d)  $t = t_1 + 0.6$ , (e)  $t = t_1 + 0.8$ , (f)  $t = t_1 + 1.0$ , (g)  $t = t_1 + 1.2$ , (h)  $t = t_1 + 1.4$ , (i)  $t = t_1 + 1.6$ , (j)  $t = t_1 + 1.8$ .  $t_1$  denotes the initial time instant in this sequence.

Before proceeding further, we first compare our simulations with previous works for an assessment and verification of the accuracy of our method. Fig. 11 shows the profiles of the local Nusselt number ( $Nu$ ) at the bottom wall for Reynolds numbers  $Re = 125$  and  $250$  from the current simulation and from the previous works of [17,46,47]. For comparison, we have employed here the same flow setting and simulation conditions as those from [47] for

this set of results. Note that these conditions are slightly different from those given above for the rest of current simulations. Specifically, here the upper wall is adiabatic with the boundary condition  $\mathbf{n} \cdot \nabla T = 0$ , and the lower wall is maintained at a constant temperature  $T_w$ . The velocity and temperature at the jet inlet are both uniform ( $u = 0$ ,  $v = -U_0$ ,  $T = T_h$ ), and the Prandtl number is fixed at  $Pr = \nu/\alpha = 0.7$  [47]. On the left and right open boundaries, we

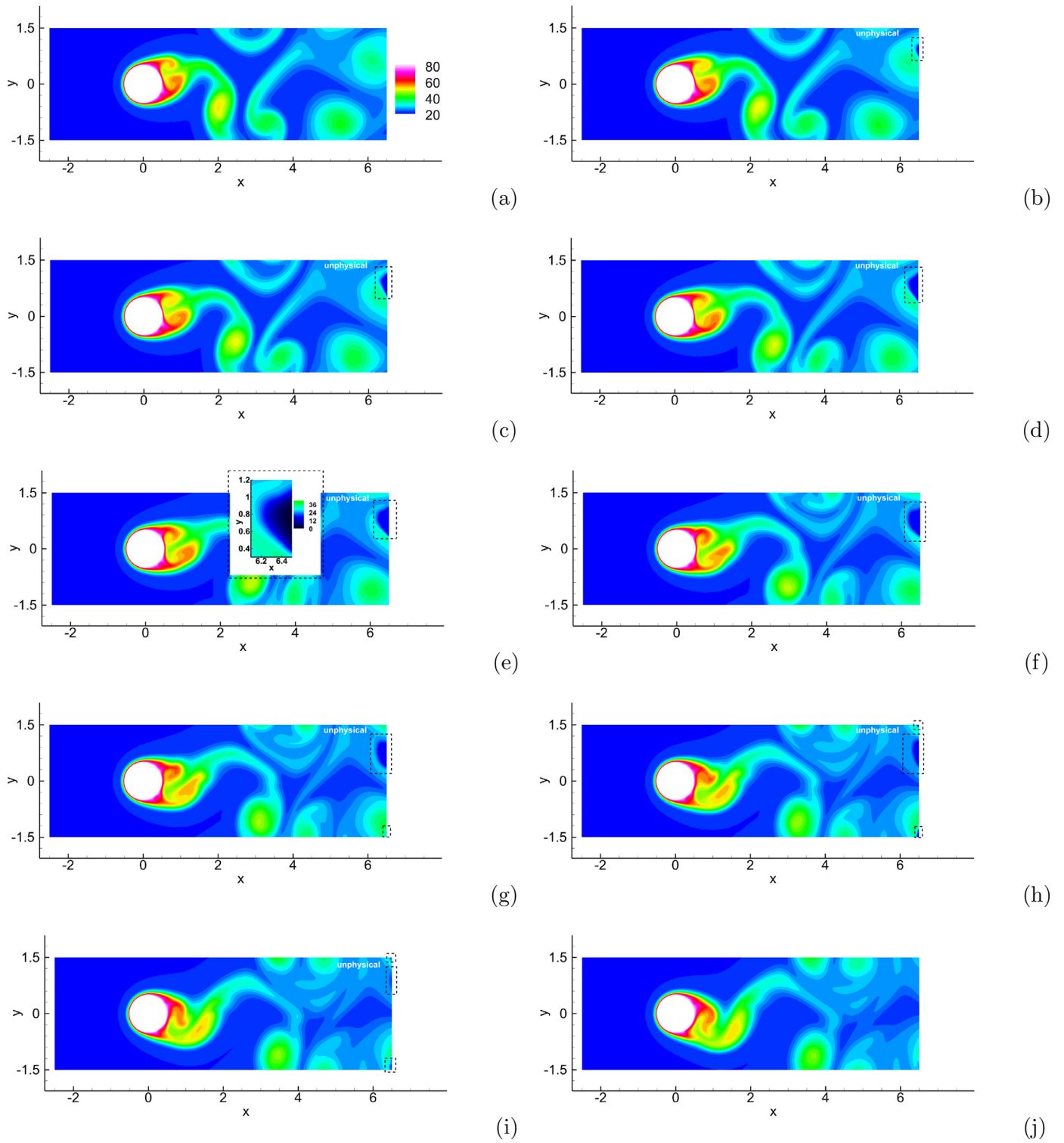


**Fig. 8.** Cylinder flow (Re=2000): temporal sequence of snapshots of the temperature distribution computed using the Neumann-type zero-flux OBC (Eq. (5)), at identical time instants as in Fig. 7. (a)  $t = t_1$ , (b)  $t = t_1 + 0.2$ , (c)  $t = t_1 + 0.4$ , (d)  $t = t_1 + 0.6$ , (e)  $t = t_1 + 0.8$ , (f)  $t = t_1 + 1.0$ , (g)  $t = t_1 + 1.2$ , (h)  $t = t_1 + 1.4$ , (i)  $t = t_1 + 1.6$ , (j)  $t = t_1 + 1.8$ . The inset of plot (e) shows a magnified view near the outflow boundary. Dashed boxes mark the regions with unphysical temperature distribution (below 20 degrees Celsius). Thermal diffusivity is  $\alpha = 0.01$ .

impose the open boundary condition (6) with  $D_0 = \frac{1}{U_0}$  and  $\delta = 0.05$  for the temperature, and the boundary condition (26) with  $\mathbf{f}_b = 0$  and  $\mathbf{E}(\mathbf{n}, \mathbf{u})$  given by (27). The local Nusselt number at the bottom wall is defined as  $Nu = \frac{1}{T_h - T_w} \frac{\partial T}{\partial y} \Big|_{y=0}$ . It is evident from

Fig. 11 that our simulation results are in good agreement with those of [17,46,47].

Let us now focus on the study of the temperature and flow features of the impinging jet. For each set of physical and simulation parameters (Reynolds number, thermal diffusivity, element order,

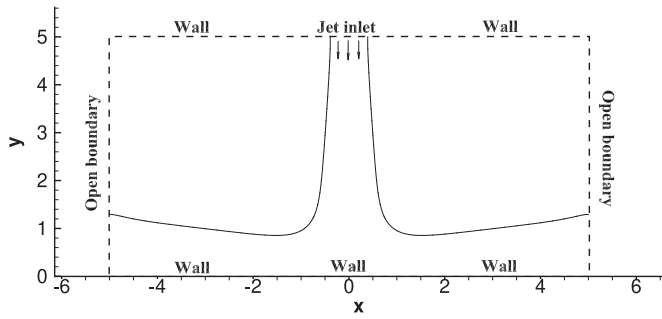


Fig. 9. Impinging jet: Flow configuration and boundary conditions.

time step size), we have performed a long-time simulation, and the flow and temperature fields of the jet have reached a statistically stationary state corresponding to that set of parameter values. Fig. 12 shows the time histories of the temperature norms  $T_{L_2}(t)$  and  $T_{H_1}(t)$  defined in Eq. (23) for the impinging jet problem. This corresponds to the Reynolds number  $Re = 2000$  and a thermal diffusivity  $\alpha = 0.01$ , and is computed with an element order 8 and a time step size  $\Delta t = 2.5e - 4$ . These temperature histories are fluctuational in time. But their values all stay around some constant mean levels, and the overall characteristics of these signals remain the same over time. These results signify that our method is long-term stable and that the temperature distribution has indeed reached a statistically stationary state.

We have computed the time-averaged mean and rms of the temperature norms based on the history data of  $T_{L_2}(t)$  and  $T_{H_1}(t)$ . Table 2 lists the mean ( $\bar{T}_{L_2}$  and  $\bar{T}_{H_1}$ ) and rms ( $T'_{L_2}$  and  $T'_{H_1}$ ) of these temperatures obtained with element orders ranging from 3 to 9. These results for two Reynolds numbers  $Re = 300$  and  $Re = 2000$ , and a thermal diffusivity  $\alpha = 0.01$ . A time step size  $\Delta t = 2.5e - 4$  is employed in these simulations. Since the flow at  $Re = 300$  is steady, shown in the table are the steady-state values and no time-averaging is performed for this Reynolds number. We observe that for  $Re = 300$ , with element orders 4 and above, the computed values for  $\bar{T}_{L_2}$  and  $\bar{T}_{H_1}$  are essentially the same (with a difference less than 0.5%). For  $Re = 2000$ , as the element order increases to 6 and

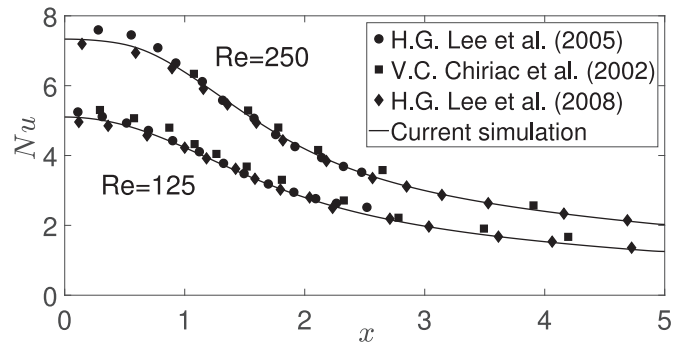


Fig. 11. Impinging jet: Comparison of the local Nusselt number at the lower wall between the current simulation and the previous works [17,46,47] for Reynolds numbers  $Re = 125$  and  $Re = 250$ . Inlet height to inlet diameter ratio is 5.

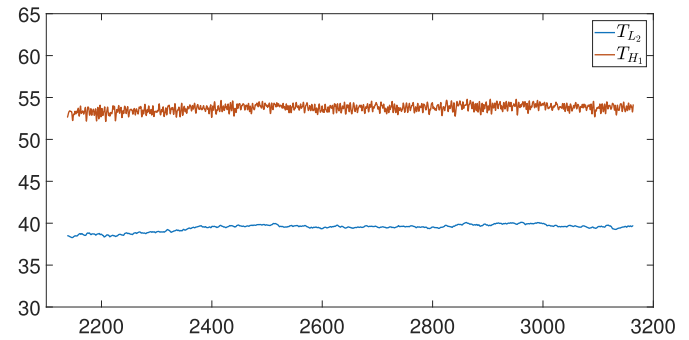


Fig. 12. Impinging jet: Time histories of  $T_{L_2}(t)$  and  $T_{H_1}(t)$  (see Eq. (23)) at Reynolds number  $Re = 2000$  and thermal diffusivity  $\alpha = 0.01$ .

above, the computed values of  $\bar{T}_{L_2}$  and  $\bar{T}_{H_1}$  become very close, exhibiting a sense of convergence.

Fig. 13 shows a comparison of the temperature profiles along the vertical direction at several horizontal locations in the domain ( $x/d = 0, 2$  and  $4$ ), computed using different element orders for  $Re = 300$  and  $\alpha = 0.01$ . It is evident that the temperature profiles corresponding to element orders 4 and above all overlap with one another, again signifying the independence of simulation results

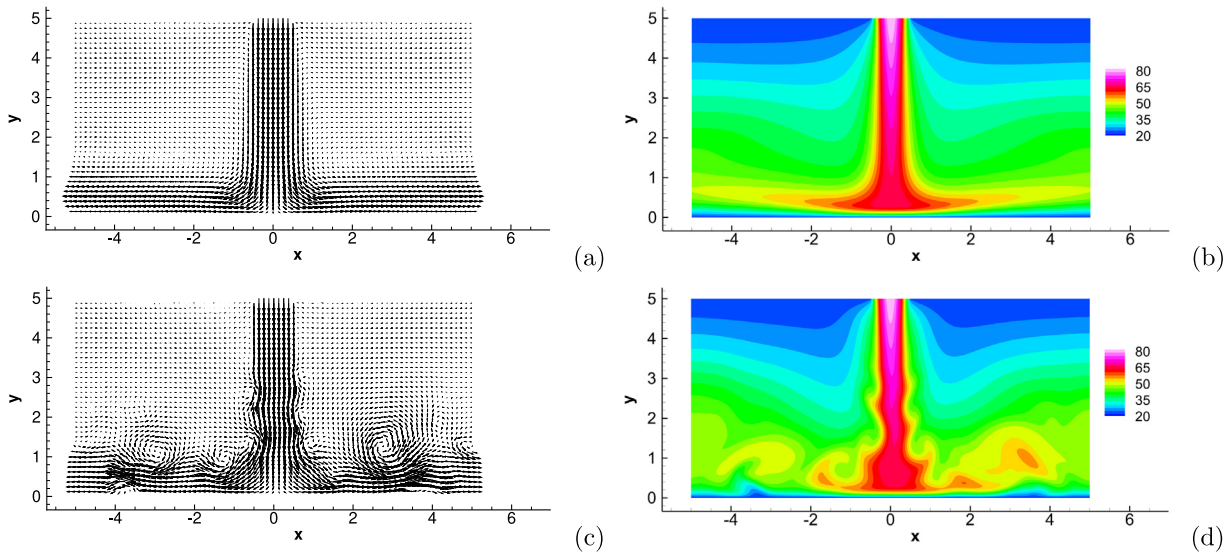
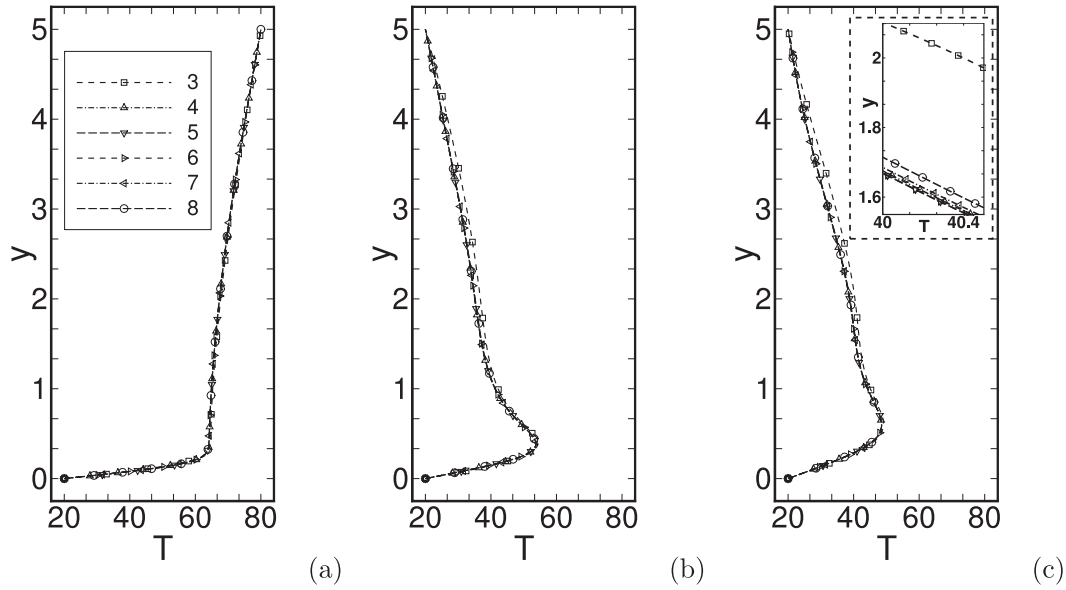


Fig. 10. Impinging jet: instantaneous velocity field (plots (a) and (c)) and temperature field (plots (b) and (d)). Plots (a) and (b) are for Reynolds number  $Re = 300$ . Plots (c) and (d) are for Reynolds number  $Re = 2000$ . Thermal diffusivity is  $\alpha = 0.01$  with both Reynolds numbers. Velocity vectors are plotted on a sparser set of mesh points for clarity.



**Fig. 13.** Impinging jet ( $Re = 300$ ): Comparison of temperature profiles along the vertical direction at three horizontal locations, (a) centerline ( $x = 0$ ), (b)  $x = 2.0$  and (c)  $x = 4.0$ , computed using element orders ranging from 3 to 8.

**Table 2**

Impinging jet: Time-averaged mean ( $\bar{T}_{L_2}$  and  $\bar{T}_{H_1}$ ) and root-mean-square (rms,  $T'_{L_2}$  and  $T'_{H_1}$ ) temperatures of  $T_{L_2}(t)$  and  $T_{H_1}(t)$  computed using various element orders. Thermal diffusivity is  $\alpha = 0.01$ .

Reynolds number	Element order	$\bar{T}_{L_2}$	$T'_{L_2}$	$\bar{T}_{H_1}$	$T'_{H_1}$
300	3	39.599	0	53.341	0
	4	38.513	0	52.611	0
	5	38.502	0	52.607	0
	6	38.498	0	52.606	0
	7	38.508	0	52.613	0
	8	38.559	0	52.645	0
2000	5	39.934	0.228	54.036	0.355
	6	39.745	0.139	53.915	0.318
	7	39.663	0.175	53.846	0.367
	8	39.703	0.135	53.887	0.356
	9	39.743	0.171	53.902	0.342

with respect to the mesh resolution. The majority of simulations reported below are performed with an element order 6 for  $Re = 300$  and element order 8 for Reynolds numbers  $Re = 2000$  and  $Re = 5000$ .

We have also performed simulations at  $Re = 300$  with several time step sizes (ranging from  $\Delta t = 1e - 3$  to  $\Delta t = 2.5e - 4$ ), and tested the sensitivity of the results with respect to  $\Delta t$ . It is observed that the obtained results corresponding to different  $\Delta t$  are basically the same. The majority of simulation results reported below are computed with a time step size  $\Delta t = 2.5e - 4$ .

We now look into the effect of the thermal open boundary condition on the simulated temperature distributions, and compare the current thermal OBC (Eq. (6)) and the Neumann-type zero-flux OBC (Eq. (5)) for the impinging jet problem. We observe that at low Reynolds numbers (such as  $Re = 300$ ) these OBCs produce approximately the same temperature distribution. However, as the Reynolds number increases to moderate and fairly large values (about  $Re = 2000$  and beyond), these OBCs exhibit disparate performance and produce quite different results for the temperature field. It is observed that the Neumann-type OBC (5) results in unphysical temperature distributions in large regions of the domain, while the current OBC (6) leads to a reasonable temperature distribution in the entire domain. These points are demonstrated by

**Figs. 14–17.** **Figs. 14** and **16** respectively show two separate temporal sequences of snapshots of the velocity fields at Reynolds number  $Re = 5000$  of the impinging jet. **Fig. 15** shows the temporal sequence of snapshots of the temperature fields corresponding to the velocity fields in **Fig. 14**, computed using the current thermal OBC (6). **Fig. 17** shows the temporal sequence of snapshots of the temperature fields corresponding to those velocity fields in **Fig. 16**, computed using the Neumann-type zero-flux OBC (5). The thermal diffusivity is  $\alpha = 0.005$ , and these results are obtained with an element order 8 and a time step size  $\Delta t = 2.5e - 4$ .

At  $Re = 5000$ , vortices are observed to constantly form and are convected along the jet streams. These vortices persist far downstream, and ultimately discharge from the domain through the left and right open boundaries (**Figs. 14** and **16**). It is further observed that, while quite weak, there is a persistent backflow on the upper portions of the left and right open boundaries (velocity vectors pointing generally inward), apparently due to the entrainment effect of the jet and the flow continuity. This characteristic is different from that of the cylinder flow in **Section 3.2**, where the backflows on the outflow boundary are transient and only occur when strong vortices pass through the open boundary.

We observe that at  $Re = 5000$  the Neumann-type zero-flux OBC (5) produces erroneous and unphysical temperature distributions in vast regions of the domain, apparently due to the strong vortices and persistent backflows on the open boundary. In **Fig. 17**, the dashed curves in each plot mark the temperature contour level  $T = 20$  degrees Celsius. The computed temperature in the regions outside the jet streams have values below 20 degrees, and in a large region the temperature is essentially zero. These results are clearly unphysical. Similar unphysical temperature distribution has been observed at  $Re = 2000$  with this boundary condition. These results indicate that, while it seems to work well at low Reynolds numbers, the Neumann-type zero-flux OBC (5) is inadequate for moderate and high Reynolds numbers, when strong vortices or backflows are present on the open boundary.

In contrast, the current thermal OBC (6) performs quite well. It produces a reasonable temperature distribution for all Reynolds numbers tested here; see **Fig. 15** for  $Re = 5000$  and **Figs. 10(b,d)**

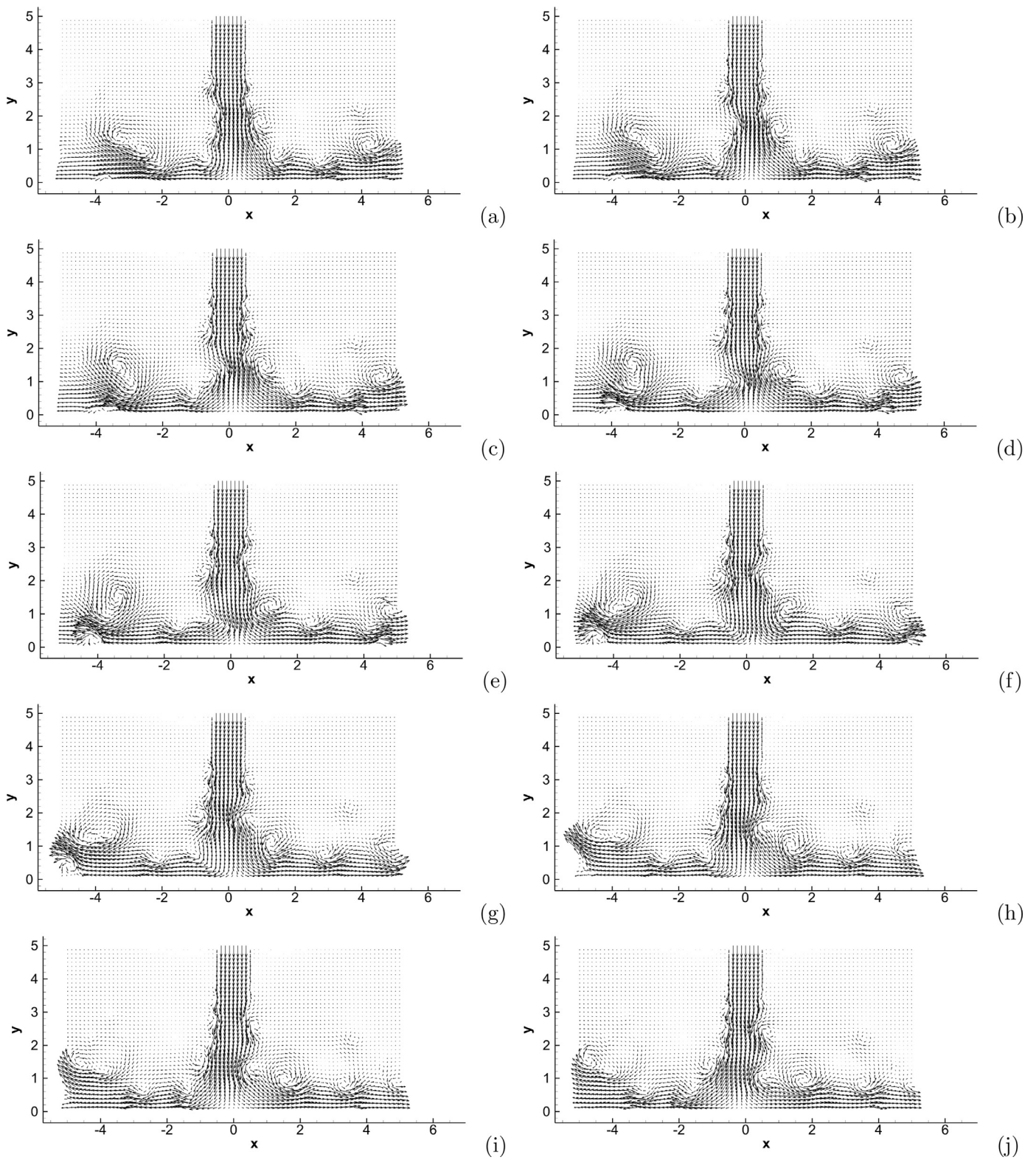


**Fig. 14.** Impinging jet ( $Re=5000$ ): temporal sequence of snapshots of the velocity distributions. (a)  $t = t_0$ , (b)  $t = t_0 + 0.5$ , (c)  $t = t_0 + 1.0$ , (d)  $t = t_0 + 1.5$ , (e)  $t = t_0 + 2.0$ , (f)  $t = t_0 + 2.5$ , (g)  $t = t_0 + 3.0$ , (h)  $t = t_0 + 3.5$ , (i)  $t = t_0 + 4.0$ , (j)  $t = t_0 + 4.5$ .  $t_0$  is the initial time instant of this sequence. Velocity vectors are plotted on a set of sparser mesh points for clarity.

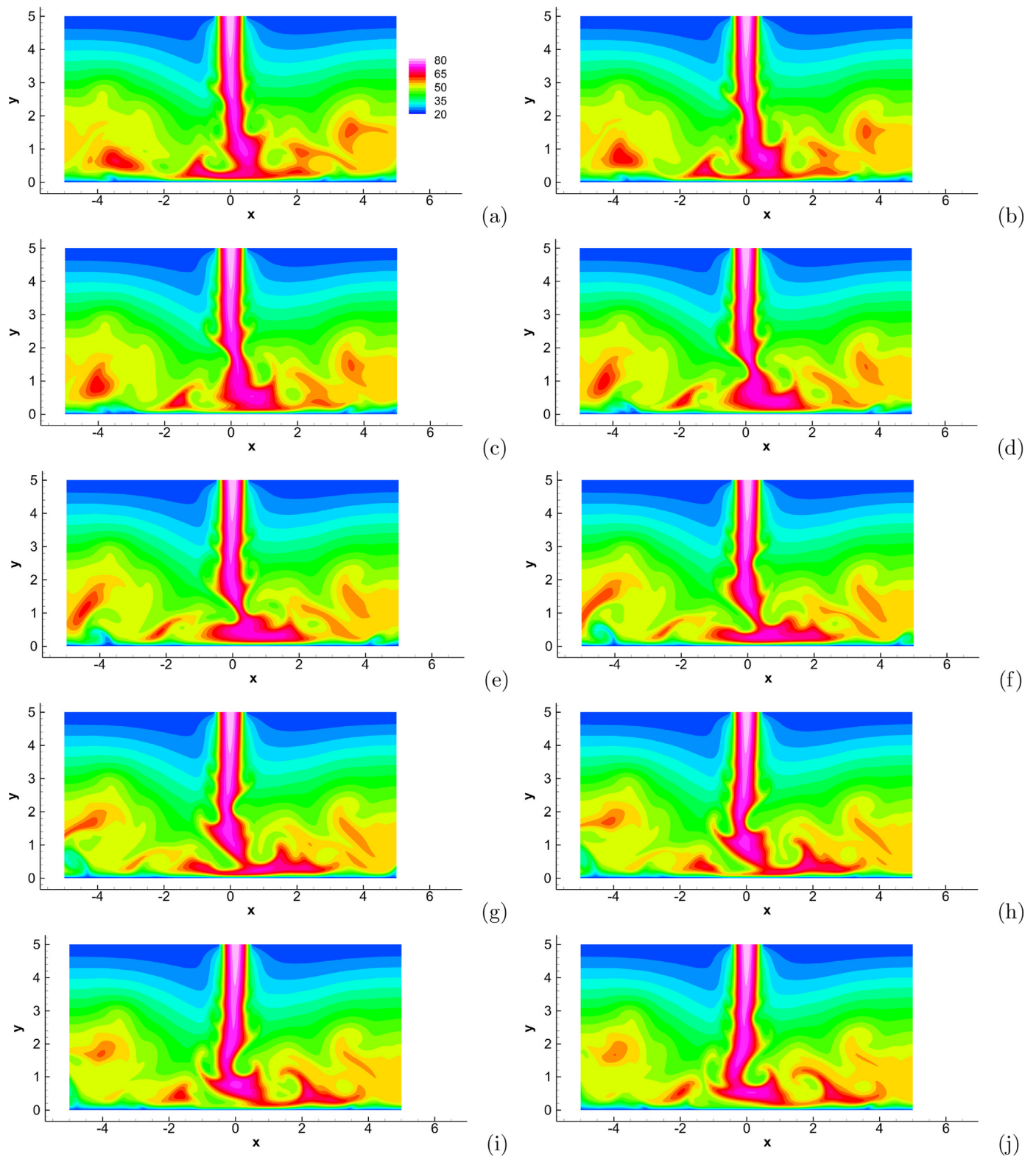


**Fig. 15.** Impinging jet ( $Re=5000$ ): temporal sequence of snapshots of the temperature distribution at identical time instants as in Fig. 14, computed using the current thermal open boundary condition. (a)  $t = t_0$ , (b)  $t = t_0 + 0.5$ , (c)  $t = t_0 + 1.0$ , (d)  $t = t_0 + 1.5$ , (e)  $t = t_0 + 2.0$ , (f)  $t = t_0 + 2.5$ , (g)  $t = t_0 + 3.0$ , (h)  $t = t_0 + 3.5$ , (i)  $t = t_0 + 4.0$ , (j)  $t = t_0 + 4.5$ . Thermal diffusivity is  $\alpha = 0.005$ .

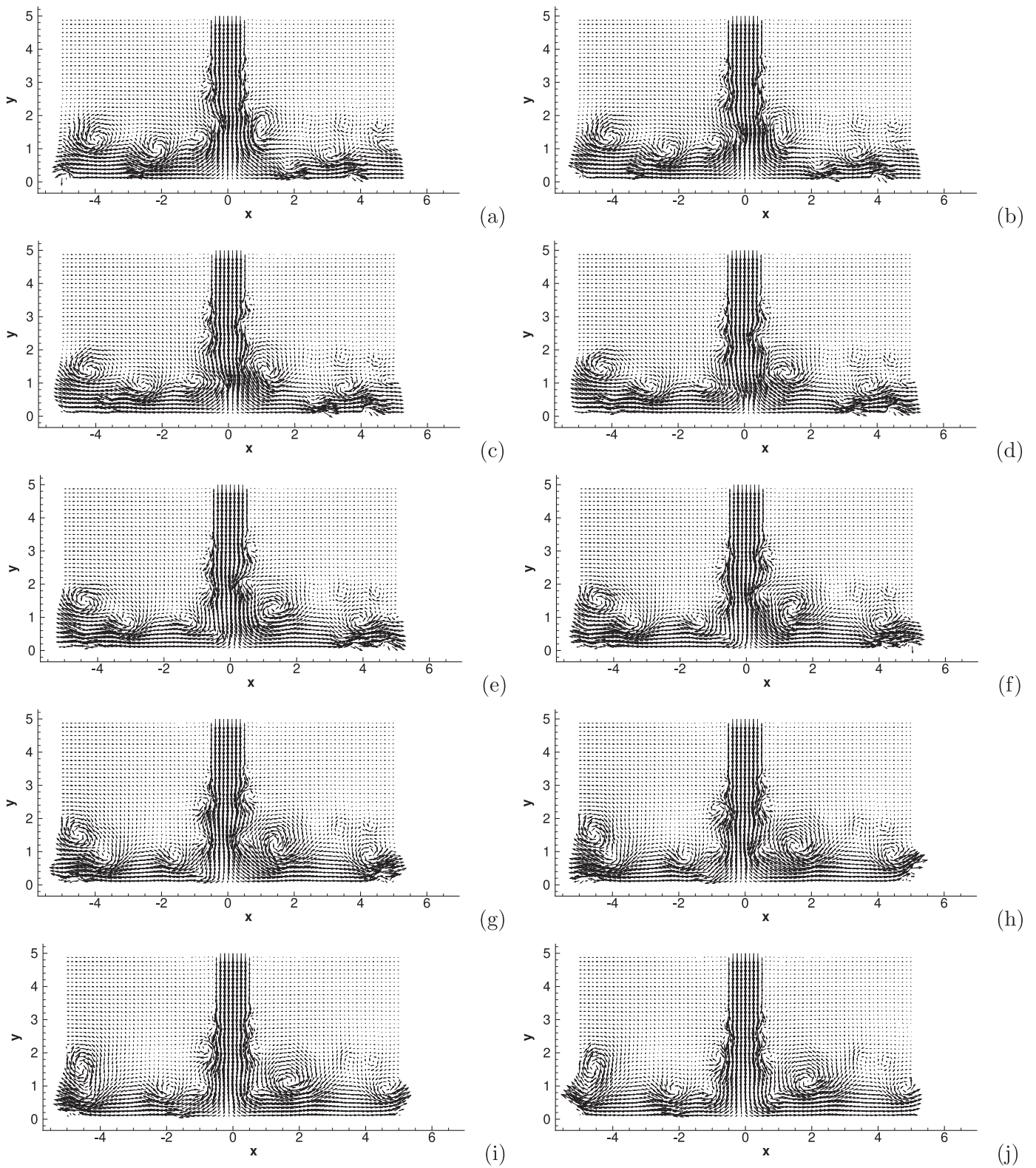


**Fig. 16.** Impinging jet ( $Re=5000$ ): another temporal sequence of snapshots of the velocity distribution. (a)  $t = t_1$ , (b)  $t = t_1 + 0.5$ , (c)  $t = t_1 + 1.0$ , (d)  $t = t_1 + 1.5$ , (e)  $t = t_1 + 2.0$ , (f)  $t = t_1 + 2.5$ , (g)  $t = t_1 + 3.0$ , (h)  $t = t_1 + 3.5$ , (i)  $t = t_1 + 4.0$ , (j)  $t = t_1 + 4.5$ .  $t_1$  is the initial time instant of this sequence. Velocity vectors are plotted on a set of sparser mesh points for clarity.

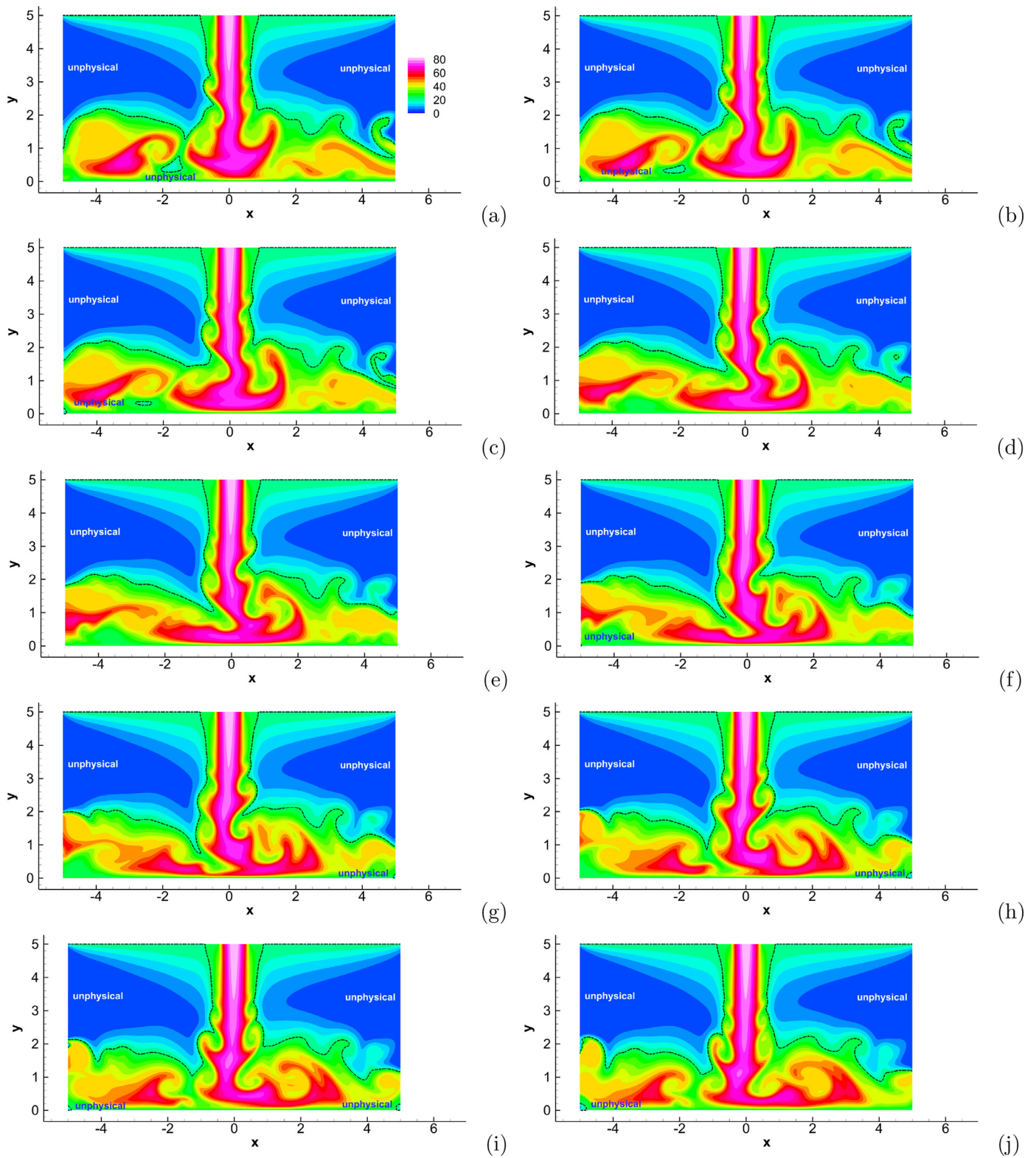


**Fig. 17.** Impinging jet ( $Re=5000$ ): temporal sequence of snapshots of the temperature distribution at identical time instants as in Fig. 16, computed using the Neumann-type zero-flux OBC (Eq. (5)). (a)  $t = t_1$ , (b)  $t = t_1 + 0.5$ , (c)  $t = t_1 + 1.0$ , (d)  $t = t_1 + 1.5$ , (e)  $t = t_1 + 2.0$ , (f)  $t = t_1 + 2.5$ , (g)  $t = t_1 + 3.0$ , (h)  $t = t_1 + 3.5$ , (i)  $t = t_1 + 4.0$ , (j)  $t = t_1 + 4.5$ . Thermal diffusivity is  $\alpha = 0.005$ . Note that the color map represents temperature values ranging from  $T = 0$  to  $T = 80$ . The dashed curves mark the contour level  $T = 20$ . The Neumann-type OBC leads to unphysical temperature distribution outside the jet stream.

for lower Reynolds numbers. The current method can handle thermal open boundaries well at moderate and high Reynolds numbers, even when strong vortices or backflows are prevalent there and pose a significant issue to other methods.

**4. Concluding remarks**

We have presented a simple and effective thermal open boundary condition for simulating convective heat transfer problems on domains involving outflows or open boundaries. This boundary condition is energy-stable, and ensures that the contribution of the open boundary will not cause an “energy-like” function of the temperature to increase over time, regardless of the flow situation that occurs on the outflow/open boundary. This open boundary condition can be implemented in a straightforward way into semi-implicit type schemes for the heat transfer equation. Ample numerical experiments show that the presented open boundary condition has a clear advantage over related methods such as the Neumann-type zero-flux condition for high (and moderate) Reynolds numbers, where strong vortices or backflows might occur on the open boundary. In the presence of strong vortices or backflows at the open boundary, the current method produces reasonable temperature distributions, while the Neumann-type zero-flux condition leads to unphysical and erroneous temperature fields. We anticipate that the presented method can be a powerful tool and be instrumental in heat transfer simulations involving in-flows/outflows at large Reynolds numbers.

**Declaration of Competing Interests**

The authors declare that they have no known competing financial interests or personal relationships that could have appeared to influence the work reported in this paper.

**CRedit authorship contribution statement**

**Xiaoyu Liu:** Software, Funding acquisition, Data curation, Visualization. **Zhi Xie:** Formal analysis. **Suchuan Dong:** Conceptualization, Methodology, Writing - review & editing.

**Acknowledgements**

This work was partially supported by NSF (DMS-1522537) and a scholarship from the China Scholarship Council (CSC-201806080040).

**Appendix A. Numerical algorithm and open boundary condition for incompressible Navier-Stokes equations**

The numerical algorithm and the open boundary conditions for the incompressible Navier-Stokes Eqs. (1a)–(1b) employed in the current work stem from our previous work [23]. This Appendix provides a summary of these aspects. We use the same notation here as in the main text.

For the Navier-Stokes Eqs. (1a)–(1b), on the boundary  $\partial\Omega_d$  ( $\partial\Omega_d = \partial\Omega_{dd} \cup \partial\Omega_{dn}$ ) we impose the Dirichlet condition

$$\mathbf{u} = \mathbf{w}(\mathbf{x}, t), \quad \text{on } \partial\Omega_d, \tag{25}$$

where  $\mathbf{w}(\mathbf{x}, t)$  is the boundary velocity. On the open boundary we impose the following condition (see [23]),

$$\nu D_0 \frac{\partial \mathbf{u}}{\partial t} - p\mathbf{n} + \nu \mathbf{n} \cdot \nabla \mathbf{u} - \mathbf{E}(\mathbf{n}, \mathbf{u}) = \mathbf{f}_b(\mathbf{x}, t), \quad \text{on } \partial\Omega_o, \tag{26}$$

where  $D_0 \geq 0$  is the same constant parameter as in the temperature condition (6), and  $\mathbf{E}(\mathbf{n}, \mathbf{u})$  is given by

$$\mathbf{E}(\mathbf{n}, \mathbf{u}) = \frac{1}{2} [(\mathbf{u} \cdot \mathbf{u})\mathbf{n} + (\mathbf{n} \cdot \mathbf{u})\mathbf{u}] \Theta_0(\mathbf{n}, \mathbf{u}). \tag{27}$$

Note that  $\Theta_0(\mathbf{n}, \mathbf{u})$  is defined in (7). A more general form for  $\mathbf{E}(\mathbf{n}, \mathbf{u})$  is given by [23],

$$\mathbf{E}(\mathbf{n}, \mathbf{u}) = \frac{1}{2} [(\beta_0 + \beta_2)(\mathbf{u} \cdot \mathbf{u})\mathbf{n} + (1 - \beta_0 + \beta_1)(\mathbf{n} \cdot \mathbf{u})\mathbf{u}] \Theta_0(\mathbf{n}, \mathbf{u}), \tag{28}$$

where  $\beta_0, \beta_1$  and  $\beta_2$  are constant parameters satisfying  $0 \leq \beta_0 \leq 1, \beta_1 \geq 0$  and  $\beta_2 \geq 0$ . The open boundary condition (26), with  $\mathbf{f}_b = 0$ , is an energy-stable boundary condition for the incompressible Navier-Stokes Eqs. (1a)–(1b) as  $\delta \rightarrow 0$  [23]. In addition, we impose the following initial condition for the velocity,

$$\mathbf{u}(\mathbf{x}, 0) = \mathbf{u}_m(\mathbf{x}) \tag{29}$$

where  $\mathbf{u}_m$  denotes the initial velocity distribution.

Given  $(\mathbf{u}^n, p^n)$  we compute  $p^{n+1}$  and  $\mathbf{u}^{n+1}$  successively in a decoupled fashion as follows: For  $p^{n+1}$  :

$$\frac{\gamma_0 \tilde{\mathbf{u}}^{n+1} - \hat{\mathbf{u}}}{\Delta t} + \mathbf{u}^{*,n+1} \cdot \nabla \mathbf{u}^{*,n+1} + \nabla p^{n+1} + \nu \nabla \times \nabla \times \mathbf{u}^{*,n+1} = \mathbf{f}^{n+1}, \tag{30a}$$

$$\nabla \cdot \tilde{\mathbf{u}}^{n+1} = 0; \tag{30b}$$

$$\mathbf{n} \cdot \tilde{\mathbf{u}}^{n+1} = \mathbf{n} \cdot \mathbf{w}^{n+1}, \quad \text{on } \partial\Omega_d; \tag{30c}$$

$$\begin{aligned} \nu D_0 \frac{\gamma_0 \tilde{\mathbf{u}}^{n+1} - \hat{\mathbf{u}}}{\Delta t} \cdot \mathbf{n} - p^{n+1} + \nu \mathbf{n} \cdot \nabla \mathbf{u}^{*,n+1} \cdot \mathbf{n} - \mathbf{n} \cdot \mathbf{E}(\mathbf{n}, \mathbf{u}^{*,n+1}) \\ = \mathbf{f}_b^{n+1} \cdot \mathbf{n}, \quad \text{on } \partial\Omega_o. \end{aligned} \tag{30d}$$

For  $\mathbf{u}^{n+1}$  :

$$\frac{\gamma_0 \mathbf{u}^{n+1} - \gamma_0 \tilde{\mathbf{u}}^{n+1}}{\Delta t} - \nu \nabla^2 \mathbf{u}^{n+1} = \nu \nabla \times \nabla \times \mathbf{u}^{*,n+1}; \tag{31a}$$

$$\mathbf{u}^{n+1} = \mathbf{w}^{n+1}, \quad \text{on } \partial\Omega_d; \tag{31b}$$

$$\begin{aligned} \nu D_0 \frac{\gamma_0 \mathbf{u}^{n+1} - \hat{\mathbf{u}}}{\Delta t} - p^{n+1} \mathbf{n} \\ + \nu \mathbf{n} \cdot \nabla \mathbf{u}^{n+1} - \mathbf{E}(\mathbf{n}, \mathbf{u}^{*,n+1}) + \nu (\nabla \cdot \mathbf{u}^{*,n+1}) \mathbf{n} = \mathbf{f}_b^{n+1}, \quad \text{on } \partial\Omega_o. \end{aligned} \tag{31c}$$

In the above equations  $\tilde{\mathbf{u}}^{n+1}$  is an auxiliary variable approximating  $\mathbf{u}^{n+1}$ . We again use  $J$  ( $J = 1$  or  $2$ ) to denote the temporal order of accuracy.  $\gamma_0$  is defined in (17).  $\hat{\mathbf{u}}$  and  $\mathbf{u}^{*,n+1}$  are defined by

$$\hat{\mathbf{u}} = \begin{cases} \mathbf{u}^n, & J = 1, \\ 2\mathbf{u}^n - \frac{1}{2}\mathbf{u}^{n-1}, & J = 2; \end{cases} \quad \mathbf{u}^{*,n+1} = \begin{cases} \mathbf{u}^n, & J = 1, \\ 2\mathbf{u}^n - \mathbf{u}^{n-1}, & J = 2. \end{cases} \tag{32}$$

The weak form for the pressure  $p^{n+1}$  can be derived from Eqs. (30a)–(30d), and it is given by [23],

$$\begin{aligned} \int_{\Omega} \nabla p^{n+1} \cdot \nabla q + \frac{1}{\nu D_0} \int_{\partial\Omega_o} p^{n+1} q = \int_{\Omega} \mathbf{G}^{n+1} \cdot \nabla q - \nu \int_{\partial\Omega_d \cup \partial\Omega_o} \\ \mathbf{n} \times \mathbf{u}^{*,n+1} \cdot \nabla q \\ + \int_{\partial\Omega_o} \left\{ -\frac{1}{\Delta t} \mathbf{n} \cdot \hat{\mathbf{u}} + \frac{1}{\nu D_0} [\nu \mathbf{n} \cdot \nabla \mathbf{u}^{*,n+1} \cdot \mathbf{n} - \mathbf{n} \cdot \mathbf{E}(\mathbf{n}, \mathbf{u}^{*,n+1}) - \mathbf{f}_b^{n+1} \cdot \mathbf{n}] \right\} q \\ - \frac{\gamma_0}{\Delta t} \int_{\partial\Omega_d} \mathbf{n} \cdot \mathbf{w}^{n+1} q, \quad \forall q \in H^1(\Omega), \end{aligned} \tag{33}$$

where  $\mathbf{G}^{n+1} = \mathbf{f}^{n+1} + \frac{\hat{\mathbf{u}}}{\Delta t} - \mathbf{u}^{*,n+1} \cdot \nabla \mathbf{u}^{*,n+1}$ . The weak form for the velocity is given by,

$$\frac{\gamma_0}{\nu \Delta t} \int_{\Omega} \mathbf{u}^{n+1} \varphi + \int_{\Omega} \nabla \varphi \cdot \nabla \mathbf{u}^{n+1} + \frac{\gamma_0 D_0}{\Delta t} \int_{\partial\Omega_o} \mathbf{u}^{n+1} \varphi = \frac{1}{\nu} \int_{\Omega}$$

$$\begin{aligned}
 & (\mathbf{G}^{n+1} - \nabla p^{n+1})\varphi \\
 & + \int_{\partial\Omega_o} \left\{ \frac{D_0}{\Delta t} \hat{\mathbf{u}} + \frac{1}{\nu} [p^{n+1} \mathbf{n} + \mathbf{E}(\mathbf{n}, \mathbf{u}^{*,n+1}) + \mathbf{f}_b^{n+1} - \nu(\nabla \cdot \mathbf{u}^{*,n+1}) \mathbf{n}] \right\} \varphi, \\
 & \forall \varphi \in H^1(\Omega) \text{ with } \varphi|_{\partial\Omega_d} = 0.
 \end{aligned} \tag{34}$$

The weak forms in (33) and (34) can be discretized using  $C^0$  spectral elements in the standard fashion [40]. Within each time step, we first solve Eq. (33) for  $p^{n+1}$ . Then we solve Eq. (34), together with the boundary condition (31b), for  $\mathbf{u}^{n+1}$ . Note that the auxiliary velocity  $\hat{\mathbf{u}}^{n+1}$  is not explicitly computed.

**Appendix B. Derivation of Equations (8) and (10)**

In this appendix we derive the energy balance Eq. (8), which corresponds to the open boundary condition (6) on  $\partial\Omega_o$ , and also the energy balance Eq. (10), which corresponds to the open boundary condition (9) on  $\partial\Omega_o$ .

As pointed out in Section 2.1, in the smoothed step function  $\Theta_0(\mathbf{n}, \mathbf{u})$  given in Eq. (7), the small positive constant  $\delta$  ( $\delta > 0$ ) controls the sharpness of this function. Note that as  $\delta$  approaches zero,  $\Theta_0(\mathbf{n}, \mathbf{u})$  approaches the step function  $\Theta_{s0}(\mathbf{n}, \mathbf{u})$ . This limit relation and the definition of  $\Theta_{s0}(\mathbf{n}, \mathbf{u})$  are given in the second part of Eq. (7). This relation will be employed in subsequent derivations. In what follows we use “as  $\delta \rightarrow 0$ ” to denote “as  $\delta$  approaches zero”.

*Derivation of Eq. (8)*

With the open boundary condition (6) on  $\partial\Omega_o$  and the assumptions in (A1), the energy balance Eq. (4) is transformed into

$$\begin{aligned}
 \frac{\partial}{\partial t} \int_{\Omega} \frac{1}{2} |T|^2 d\Omega &= -\alpha \int_{\Omega} |\nabla T|^2 d\Omega + \int_{\partial\Omega_o} \frac{1}{2} (\mathbf{n} \cdot \mathbf{u}) T^2 \\
 & [2\Theta_0(\mathbf{n}, \mathbf{u}) - 1] dA - \alpha D_0 \int_{\partial\Omega_o} \frac{\partial}{\partial t} \left( \frac{1}{2} T^2 \right) dA.
 \end{aligned} \tag{35}$$

Let  $\delta \rightarrow 0$  in the open boundary condition (6). Note that  $\lim_{\delta \rightarrow 0} \Theta_0(\mathbf{n}, \mathbf{u}) = \Theta_{s0}(\mathbf{n}, \mathbf{u})$  (see Eq. (7)). Then as  $\delta \rightarrow 0$ , Eq. (35) is reduced to

$$\begin{aligned}
 \frac{\partial}{\partial t} \left( \int_{\Omega} \frac{1}{2} |T|^2 d\Omega + \alpha D_0 \int_{\partial\Omega_o} \frac{1}{2} |T|^2 dA \right) &= -\alpha \int_{\Omega} |\nabla T|^2 d\Omega \\
 & + \int_{\partial\Omega_o} \frac{1}{2} (\mathbf{n} \cdot \mathbf{u}) T^2 [2\Theta_{s0}(\mathbf{n}, \mathbf{u}) - 1] dA,
 \end{aligned} \tag{36}$$

where we have moved the last term on the right hand side of Eq. (35) to the left hand side.

In light of the definition of  $\Theta_{s0}(\mathbf{n}, \mathbf{u})$  in Eq. (7), the last term on the right hand side of Eq. (36) can be transformed into

$$\begin{aligned}
 & \frac{1}{2} (\mathbf{n} \cdot \mathbf{u}) T^2 [2\Theta_{s0}(\mathbf{n}, \mathbf{u}) - 1] \\
 & = \begin{cases} -\frac{1}{2} (\mathbf{n} \cdot \mathbf{u}) T^2 = -\frac{1}{2} |\mathbf{n} \cdot \mathbf{u}| T^2, & \text{if } \mathbf{n} \cdot \mathbf{u} > 0; \\ 0 & = -\frac{1}{2} |\mathbf{n} \cdot \mathbf{u}| T^2, & \text{if } \mathbf{n} \cdot \mathbf{u} = 0; \\ \frac{1}{2} (\mathbf{n} \cdot \mathbf{u}) T^2 = -\frac{1}{2} |\mathbf{n} \cdot \mathbf{u}| T^2, & \text{if } \mathbf{n} \cdot \mathbf{u} < 0. \end{cases}
 \end{aligned} \tag{37}$$

Therefore, Eq. (36) is reduced to, as  $\delta \rightarrow 0$ ,

$$\begin{aligned}
 \frac{\partial}{\partial t} \left( \int_{\Omega} \frac{1}{2} |T|^2 d\Omega + \alpha D_0 \int_{\partial\Omega_o} \frac{1}{2} |T|^2 dA \right) \\
 = -\alpha \int_{\Omega} |\nabla T|^2 d\Omega - \int_{\partial\Omega_o} \frac{1}{2} |\mathbf{n} \cdot \mathbf{u}| T^2 dA.
 \end{aligned} \tag{38}$$

Eq. (8) is the combination of Eqs. (36) and (38).

*Derivation of Eq. (10)*

With the open boundary condition (9) (with  $\theta \geq 1$ ) on  $\partial\Omega_o$  and the assumptions in (A1), the energy balance Eq. (4) can be transformed into

$$\begin{aligned}
 \frac{\partial}{\partial t} \int_{\Omega} \frac{1}{2} |T|^2 d\Omega &= -\alpha \int_{\Omega} |\nabla T|^2 d\Omega \\
 & + \int_{\partial\Omega_o} \frac{1}{2} (\mathbf{n} \cdot \mathbf{u}) T^2 [\theta \Theta_0(\mathbf{n}, \mathbf{u}) - 1] dA \\
 & - \alpha D_0 \int_{\partial\Omega_o} \frac{\partial}{\partial t} \left( \frac{1}{2} T^2 \right) dA.
 \end{aligned} \tag{39}$$

As  $\delta \rightarrow 0$ , this equation is reduced to

$$\begin{aligned}
 \frac{\partial}{\partial t} \left( \int_{\Omega} \frac{1}{2} |T|^2 d\Omega + \alpha D_0 \int_{\partial\Omega_o} \frac{1}{2} |T|^2 dA \right) \\
 = -\alpha \int_{\Omega} |\nabla T|^2 d\Omega + \int_{\partial\Omega_o} \frac{1}{2} (\mathbf{n} \cdot \mathbf{u}) T^2 [\theta \Theta_{s0}(\mathbf{n}, \mathbf{u}) - 1] dA.
 \end{aligned} \tag{40}$$

Let us focus on the last term on the right hand side of equation (40). In light of the definition of  $\Theta_{s0}(\mathbf{n}, \mathbf{u})$  given in (7) and the condition  $\theta \geq 1$ , this term can be reduced to

$$\frac{1}{2} (\mathbf{n} \cdot \mathbf{u}) T^2 [\theta \Theta_{s0}(\mathbf{n}, \mathbf{u}) - 1] = \begin{cases} -\frac{1}{2} (\mathbf{n} \cdot \mathbf{u}) T^2 \leq 0, & \text{if } \mathbf{n} \cdot \mathbf{u} > 0; \\ 0, & \text{if } \mathbf{n} \cdot \mathbf{u} = 0; \\ \frac{\theta-1}{2} (\mathbf{n} \cdot \mathbf{u}) T^2 \leq 0, & \text{if } \mathbf{n} \cdot \mathbf{u} < 0. \end{cases} \tag{41}$$

We then conclude that, with  $\theta \geq 1$ ,

$$\int_{\partial\Omega_o} \frac{1}{2} (\mathbf{n} \cdot \mathbf{u}) T^2 [\theta \Theta_{s0}(\mathbf{n}, \mathbf{u}) - 1] dA \leq 0. \tag{42}$$

Therefore we attain from Eq. (40) the following inequality, as  $\delta \rightarrow 0$ ,

$$\frac{\partial}{\partial t} \left( \int_{\Omega} \frac{1}{2} |T|^2 d\Omega + \alpha D_0 \int_{\partial\Omega_o} \frac{1}{2} |T|^2 dA \right) \leq -\alpha \int_{\Omega} |\nabla T|^2 d\Omega. \tag{43}$$

Eq. (10) is a combination of (40) and (43).

**Appendix C. Proof of Theorem 2.1**

In this Appendix we provide a proof of Theorem 2.1. We will first state and prove several lemmas, which then lead to the proof of Theorem 2.1. In what follows we consider the open boundary condition (9) with  $\theta \geq 1$  on  $\partial\Omega_o$ ,  $\mathbf{n}$  is the outward-pointing unit vector normal to  $\partial\Omega_o$ , and  $\Theta_0(\mathbf{n}, \mathbf{u})$  and  $\Theta_{s0}(\mathbf{n}, \mathbf{u})$  are defined in Eq. (7).

**Lemma C.1.**  $|\Theta_0(\mathbf{n}, \mathbf{u}) - \Theta_{s0}(\mathbf{n}, \mathbf{u})| < \frac{1}{2}$  for all  $\delta > 0$ .

This can be proved by straightforward verification.

**Lemma C.2.** (a) If  $\mathbf{n} \cdot \mathbf{u} = 0$ , then  $\Theta_0(\mathbf{n}, \mathbf{u}) = \Theta_{s0}(\mathbf{n}, \mathbf{u})$  for all  $\delta > 0$ . (b) Given any  $\epsilon \geq \frac{1}{2}$ ,  $|\Theta_0(\mathbf{n}, \mathbf{u}) - \Theta_{s0}(\mathbf{n}, \mathbf{u})| < \epsilon$  for all  $\delta > 0$ . (c) Suppose  $\mathbf{n} \cdot \mathbf{u} \neq 0$ . Given any  $\epsilon \in (0 < \epsilon < \frac{1}{2})$ , there exists a  $\delta_0 = \frac{|\mathbf{n} \cdot \mathbf{u}|}{U_0 \tanh^{-1}(1-2\epsilon)}$  such that for all  $0 < \delta < \delta_0$ ,  $|\Theta_0(\mathbf{n}, \mathbf{u}) - \Theta_{s0}(\mathbf{n}, \mathbf{u})| < \epsilon$ .

**Proof.** Part (a) can be verified readily. Part (b) follows from Lemma Appendix C.1. We next show that part (c) is true.

The expression for  $\delta_0$  can be transformed into  $\epsilon = \frac{1}{2} \left( 1 - \tanh \frac{|\mathbf{n} \cdot \mathbf{u}|}{U_0 \delta_0} \right)$ .

• If  $\mathbf{n} \cdot \mathbf{u} > 0$ ,  $\epsilon = \frac{1}{2} \left( 1 - \tanh \frac{\mathbf{n} \cdot \mathbf{u}}{U_0 \delta_0} \right)$ . Then  $\Theta_0(\mathbf{n}, \mathbf{u}) - \Theta_{s0}(\mathbf{n}, \mathbf{u}) = \frac{1}{2} \left( 1 - \tanh \frac{\mathbf{n} \cdot \mathbf{u}}{U_0 \delta} \right) > 0$ . So for all  $0 < \delta < \delta_0$ ,

$$0 < \Theta_0(\mathbf{n}, \mathbf{u}) - \Theta_{s0}(\mathbf{n}, \mathbf{u}) < \frac{1}{2} \left( 1 - \tanh \frac{\mathbf{n} \cdot \mathbf{u}}{U_0 \delta_0} \right) = \epsilon.$$

- If  $\mathbf{n} \cdot \mathbf{u} < 0$ ,  $\epsilon = \frac{1}{2} \left( 1 + \tanh \frac{\mathbf{n} \cdot \mathbf{u}}{U_0 \delta_0} \right)$ . Then  $\Theta_0(\mathbf{n}, \mathbf{u}) - \Theta_{s0}(\mathbf{n}, \mathbf{u}) = -\frac{1}{2} \left( 1 + \tanh \frac{\mathbf{n} \cdot \mathbf{u}}{U_0 \delta_0} \right) < 0$ . So for all  $0 < \delta < \delta_0$ ,  
 $0 > \Theta_0(\mathbf{n}, \mathbf{u}) - \Theta_{s0}(\mathbf{n}, \mathbf{u}) > -\frac{1}{2} \left( 1 + \tanh \frac{\mathbf{n} \cdot \mathbf{u}}{U_0 \delta_0} \right) = -\epsilon$ .

Combining the above, we conclude that  $|\Theta_0(\mathbf{n}, \mathbf{u}) - \Theta_{s0}(\mathbf{n}, \mathbf{u})| < \epsilon$  for all  $0 < \delta < \delta_0$ . □

This Lemma proves the limit relation between  $\Theta_0(\mathbf{n}, \mathbf{u})$  and  $\Theta_{s0}(\mathbf{n}, \mathbf{u})$  given in Eq. (7).

**Definition C.1.** We define the following quantities:

$$T_m = \max_{\mathbf{x} \in \partial\Omega_o} \{ |T(\mathbf{x}, t)| \}, \quad (\text{maximum temperature magnitude on } \partial\Omega_o); \quad (44a)$$

$$U_m = \max_{\mathbf{x} \in \partial\Omega_o} \{ |\mathbf{n} \cdot \mathbf{u}(\mathbf{x}, t)| \}; \quad (\text{maximum normal velocity magnitude on } \partial\Omega_o); \quad (44b)$$

$$A_0 = \int_{\partial\Omega_o} dA, \quad (\text{area of open boundary}); \quad (44c)$$

$$I_0(t) = \int_{\partial\Omega_o} \frac{1}{2} (\mathbf{n} \cdot \mathbf{u}) T^2 [\theta \Theta_0(\mathbf{n}, \mathbf{u}) - 1] dA; \quad (44d)$$

$$I_{s0}(t) = \int_{\partial\Omega_o} \frac{1}{2} (\mathbf{n} \cdot \mathbf{u}) T^2 [\theta \Theta_{s0}(\mathbf{n}, \mathbf{u}) - 1] dA; \quad (44e)$$

$$I(t) = I_0(t) - I_{s0}(t) = \int_{\partial\Omega_o} \frac{1}{2} (\mathbf{n} \cdot \mathbf{u}) T^2 \theta [\Theta_0(\mathbf{n}, \mathbf{u}) - \Theta_{s0}(\mathbf{n}, \mathbf{u})] dA. \quad (44f)$$

If  $T_m = 0$  or  $U_m = 0$ , then  $T \equiv 0$  or  $\mathbf{n} \cdot \mathbf{u} \equiv 0$  (identically zero) on  $\partial\Omega_o$ , and  $I_0(t) = I_{s0}(t) = I(t) = 0$  for all  $\delta > 0$ . We next assume that  $T_m > 0$  and  $U_m > 0$ .

**Definition C.2.** Let  $\epsilon > 0$  denote a given constant. We define:

$$\partial\Omega_o^a(\epsilon) = \left\{ \text{regions of } \partial\Omega_o \text{ with } |\mathbf{n} \cdot \mathbf{u}| < \frac{2\epsilon}{\theta T_m^2 A_0} \right\}; \quad (45a)$$

$$\partial\Omega_o^b(\epsilon) = \left\{ \text{regions of } \partial\Omega_o \text{ with } |\mathbf{n} \cdot \mathbf{u}| \geq \frac{2\epsilon}{\theta T_m^2 A_0} \right\}; \quad (45b)$$

$$I^a(\epsilon) = \int_{\partial\Omega_o^a(\epsilon)} \frac{1}{2} (\mathbf{n} \cdot \mathbf{u}) T^2 \theta [\Theta_0(\mathbf{n}, \mathbf{u}) - \Theta_{s0}(\mathbf{n}, \mathbf{u})] dA; \quad (45c)$$

$$I^b(\epsilon) = \int_{\partial\Omega_o^b(\epsilon)} \frac{1}{2} (\mathbf{n} \cdot \mathbf{u}) T^2 \theta [\Theta_0(\mathbf{n}, \mathbf{u}) - \Theta_{s0}(\mathbf{n}, \mathbf{u})] dA. \quad (45d)$$

Note that  $\partial\Omega_o^a$  and  $\partial\Omega_o^b$  do not overlap,  $\partial\Omega_o = \partial\Omega_o^a \cup \partial\Omega_o^b$ , and  $I(t) = I^a(\epsilon) + I^b(\epsilon)$ .

**Lemma C.3.** Given any  $\epsilon > 0$ , there exists a

$$\delta_0 = \frac{\frac{2\epsilon}{\theta T_m^2 A_0}}{U_0 \tanh^{-1}(1 - 2\epsilon_1)}, \quad \text{where } \epsilon_1 = \min \left\{ \frac{1}{3}, \frac{\epsilon}{\theta T_m^2 U_m A_0} \right\}, \quad (46)$$

such that for all  $0 < \delta < \delta_0$ ,

$$(a) |I^a(\epsilon)| < \frac{\epsilon}{2}; \quad (b) |I^b(\epsilon)| < \frac{\epsilon}{2}. \quad (47)$$

**Proof.** For any given  $\epsilon > 0$ , note that  $|\mathbf{n} \cdot \mathbf{u}| < \frac{2\epsilon}{\theta T_m^2 A_0}$  on  $\partial\Omega_o^a(\epsilon)$ , and  $|\mathbf{n} \cdot \mathbf{u}| \geq \frac{2\epsilon}{\theta T_m^2 A_0}$  on  $\partial\Omega_o^b(\epsilon)$ .

In light of (45c), we have

$$\begin{aligned} |I^a(\epsilon)| &\leq \int_{\partial\Omega_o^a(\epsilon)} \frac{1}{2} |\mathbf{n} \cdot \mathbf{u}| T^2 \theta |\Theta_0(\mathbf{n}, \mathbf{u}) - \Theta_{s0}(\mathbf{n}, \mathbf{u})| dA \\ &< \frac{\theta}{4} T_m^2 \int_{\partial\Omega_o^a(\epsilon)} |\mathbf{n} \cdot \mathbf{u}| dA < \frac{\epsilon}{2A_0} \int_{\partial\Omega_o^a(\epsilon)} dA \\ dA &\leq \frac{\epsilon}{2A_0} \int_{\partial\Omega_o} dA = \frac{\epsilon}{2}, \end{aligned} \quad (48)$$

where we have used Lemma Appendix C.1, (44a)–(44c), and (45a).

In light of (46) and (45b), we find that on  $\partial\Omega_o^b(\epsilon)$ ,

$$\delta_0 = \frac{\frac{2\epsilon}{\theta T_m^2 A_0}}{U_0 \tanh^{-1}(1 - 2\epsilon_1)} \leq \frac{|\mathbf{n} \cdot \mathbf{u}|}{U_0 \tanh^{-1}(1 - 2\epsilon_1)}. \quad (49)$$

Then based on Lemma Appendix C.2 we conclude that for all  $0 < \delta < \delta_0$ ,

$$|\Theta_0(\mathbf{n}, \mathbf{u}) - \Theta_{s0}(\mathbf{n}, \mathbf{u})| < \epsilon_1 \leq \frac{\epsilon}{\theta T_m^2 U_m A_0}, \quad \text{on } \partial\Omega_o^b(\epsilon). \quad (50)$$

In light of (45d), we have

$$\begin{aligned} |I^b(\epsilon)| &\leq \int_{\partial\Omega_o^b(\epsilon)} \frac{1}{2} |\mathbf{n} \cdot \mathbf{u}| T^2 \theta |\Theta_0(\mathbf{n}, \mathbf{u}) - \Theta_{s0}(\mathbf{n}, \mathbf{u})| dA \\ &\leq \frac{\theta}{2} U_m T_m^2 \int_{\partial\Omega_o^b(\epsilon)} |\Theta_0(\mathbf{n}, \mathbf{u}) - \Theta_{s0}(\mathbf{n}, \mathbf{u})| dA < \frac{\epsilon}{2A_0} \int_{\partial\Omega_o^b(\epsilon)} dA \\ dA &\leq \frac{\epsilon}{2A_0} \int_{\partial\Omega_o} dA = \frac{\epsilon}{2}, \end{aligned} \quad (51)$$

where we have used (44a)–(44c) and (50). □

**Lemma C.4.** Given any  $\epsilon > 0$ , with  $\delta_0$  given by Eq. (46), we have for all  $0 < \delta < \delta_0$ ,  $|I_0(t) - I_{s0}(t)| < \epsilon$ .

**Proof.** Invoking Lemma Appendix C.3, for all  $0 < \delta < \delta_0$  we have  $|I_0(t) - I_{s0}(t)| = |I^a(\epsilon) + I^b(\epsilon)| \leq |I^a(\epsilon)| + |I^b(\epsilon)| < \frac{\epsilon}{2} + \frac{\epsilon}{2} = \epsilon$ . □

Lemma Appendix C.4 implies that  $\lim_{\delta \rightarrow 0} I_0(t) = I_{s0}(t)$ .

**Definition C.3.** We define the following regions on  $\partial\Omega_o$ :

$$\partial\Omega_o^+ = \{ \text{regions of } \partial\Omega_o \text{ with } \mathbf{n} \cdot \mathbf{u} > 0 \}; \quad (52a)$$

$$\partial\Omega_o^- = \{ \text{regions of } \partial\Omega_o \text{ with } \mathbf{n} \cdot \mathbf{u} < 0 \}; \quad (52b)$$

$$\partial\Omega_o^0 = \{ \text{regions of } \partial\Omega_o \text{ with } \mathbf{n} \cdot \mathbf{u} = 0 \}. \quad (52c)$$

Note that the regions  $\partial\Omega_o^+$ ,  $\partial\Omega_o^-$  and  $\partial\Omega_o^0$  do not overlap, and that  $\partial\Omega_o = \partial\Omega_o^+ \cup \partial\Omega_o^- \cup \partial\Omega_o^0$ .

**Lemma C.5.** With  $\theta \geq 1$ ,

$$I_{s0}(t) = - \left[ \int_{\partial\Omega_o^+} \frac{1}{2} |\mathbf{n} \cdot \mathbf{u}| T^2 dA + (\theta - 1) \int_{\partial\Omega_o^-} \frac{1}{2} |\mathbf{n} \cdot \mathbf{u}| T^2 dA \right] \leq 0. \quad (53)$$

**Proof.** This conclusion follows from Eqs. (44e) and (41). □

**Theorem C.6.** For the open boundary condition (9) with  $\theta > 1$  on  $\partial\Omega_o$ , there exists a  $\delta_0 = \delta_0(\mathbf{u}, T) > 0$  such that for all  $0 < \delta < \delta_0$ ,

$$I_0(t) = \int_{\partial\Omega_o} \frac{1}{2} (\mathbf{n} \cdot \mathbf{u}) T^2 [\theta \Theta_0(\mathbf{n}, \mathbf{u}) - 1] dA \leq 0. \quad (54)$$

**Proof.** If  $(\mathbf{n} \cdot \mathbf{u}) T^2 \equiv 0$  (identically zero) on  $\partial\Omega_o$ , then  $I_0(t) = 0$  for all  $\delta > 0$ , and the conclusion is true.

Let us now assume that  $(\mathbf{n} \cdot \mathbf{u})T^2$  is not identically zero on  $\partial\Omega_o$ . Then  $U_m > 0$ ,  $T_m > 0$ , and  $\int_{\partial\Omega_o} |\mathbf{n} \cdot \mathbf{u}|T^2 dA > 0$ . Let

$$\epsilon = \int_{\partial\Omega_o^+} \frac{1}{2} |\mathbf{n} \cdot \mathbf{u}|T^2 dA + (\theta - 1) \int_{\partial\Omega_o^-} \frac{1}{2} |\mathbf{n} \cdot \mathbf{u}|T^2 dA. \tag{55}$$

Then  $\epsilon > 0$ , and in light of Lemma Appendix C.5,

$$I_{s0}(t) = -\epsilon. \tag{56}$$

Let  $\delta_0$  be given by Eq. (46), in which  $\epsilon$  is given by (55). Then for all  $0 < \delta < \delta_0$ ,  $|I_0(t) - I_{s0}(t)| < \epsilon$  according to Lemma Appendix C.4. Therefore, for all  $0 < \delta < \delta_0$ ,

$$I_0(t) = I_{s0}(t) + [I_0(t) - I_{s0}(t)] = -\epsilon + [I_0(t) - I_{s0}(t)] \leq -\epsilon + |I_0(t) - I_{s0}(t)| < -\epsilon + \epsilon = 0. \quad \square$$

Theorem 2.1 follows from Theorem Appendix C.6 and Eq. (39).

The Case with  $\theta = 1$

In Theorems Appendix C.6 and 2.1 we have excluded the case with  $\theta = 1$  for the open boundary condition (9) on  $\partial\Omega_o$ . We next briefly discuss the case with  $\theta = 1$ .

We only need to consider the situation in which  $(\mathbf{n} \cdot \mathbf{u})T^2$  is not identically zero on  $\partial\Omega_o$ . Then  $U_m > 0$ ,  $T_m > 0$  and  $\int_{\partial\Omega_o} |\mathbf{n} \cdot \mathbf{u}|T^2 dA > 0$ . With  $\theta = 1$ , Eq. (53) is reduced to

$$I_{s0}(t) = - \int_{\partial\Omega_o^+} \frac{1}{2} |\mathbf{n} \cdot \mathbf{u}|T^2 dA \leq 0. \tag{57}$$

If  $I_{s0}(t) < 0$ , then this case can be dealt with in the same way as for  $\theta > 1$ , and the proof for Theorem Appendix C.6 can be applied here for  $\theta = 1$ . So we conclude that  $I_0(t) < 0$  for all  $0 < \delta < \delta_0$  with  $\delta_0$  given by (46), in which  $\epsilon = \int_{\partial\Omega_o^+} \frac{1}{2} |\mathbf{n} \cdot \mathbf{u}|T^2 dA$ .

Let us now focus on the situation  $I_{s0}(t) = 0$ . This is possible because the region  $\partial\Omega_o^+$  may not exist, or  $(\mathbf{n} \cdot \mathbf{u})T^2$  may be identically zero on  $\partial\Omega_o^+$ . In this case we cannot conclude that  $I_0(t) \leq 0$  anymore. However, we can still show that, for all  $0 < \delta < \delta_0$  with some  $\delta_0 > 0$ ,

$$\begin{aligned} \frac{\partial}{\partial t} \left( \int_{\Omega} \frac{1}{2} |T|^2 d\Omega + \alpha D_0 \int_{\partial\Omega_o} \frac{1}{2} |T|^2 dA \right) \\ = -\alpha \int_{\Omega} |\nabla T|^2 d\Omega + I_0(t) \leq 0. \end{aligned} \tag{58}$$

Note that the equality in the above relation stems from Eq. (39).

If the temperature is a uniform field, then by subtracting this uniform temperature during non-dimensionalization, we conclude that the non-dimensional temperature  $T = 0$ , and thus  $I_0(t) = 0$ . So the relation (58) holds. In the following we assume that  $T$  is not uniform and  $\nabla T$  is not identically zero on  $\Omega$ . Let

$$\epsilon = \alpha \int_{\Omega} |\nabla T|^2 d\Omega. \tag{59}$$

Then  $\epsilon > 0$ . Let  $\delta_0$  be given by Eq. (46), in which  $\epsilon$  is given by (59). Then by Lemma Appendix C.4, for all  $0 < \delta < \delta_0$ , we have  $|I_0(t) - I_{s0}(t)| < \epsilon$ . It follows that

$$\begin{aligned} -\alpha \int_{\Omega} |\nabla T|^2 d\Omega + I_0(t) = -\epsilon + [I_0(t) - I_{s0}(t)] \leq -\epsilon \\ + |I_0(t) - I_{s0}(t)| < -\epsilon + \epsilon = 0. \end{aligned} \tag{60}$$

So the inequality in (58) holds.

References

[1] H. Abbassi, S. Turki, S. Nasrallah, Numerical investigation of forced convection in a plane channel with a built-in triangular prism, *Int. J. Therm. Sci.* 40 (2001) 649–658.  
 [2] R. Arndt, A. Ceretani, C. Rautenberg, Heat-conducting fluids in domains with open boundaries, arXiv:1910.03994 (2019).

[3] Y. Bazilevs, J. Hohean, T. Hughes, R. Moser, Y. Zhang, Patient-specific isogeometric fluid–structure interaction analysis of therapeutic aortic blood flow due to impantation of the jarvik 2000 left ventricular assist device, *Comput. Methods Appl. Mech. Eng.* 198 (2009) 3534–3550.  
 [4] M. Behr, J. Liou, R. Shih, T. Tezduyar, Vorticity-streamfunction formulation of unsteady incompressible flow past a cylinder: sensitivity of the computed flow field to the location of the outflow boundary, *Int. J. Numer. Methods Fluids* 12 (1991) 323–342.  
 [5] M. Benes, The “do-nothing” problems for Boussinesq fluids, *Appl. Math. Lett.* 31 (2014) 25–28.  
 [6] M. Benes, I. Paganin, On existence, regularity and uniqueness of thermally coupled incompressible flows in a system of three dimensional pipes, *Nonlinear Anal.* 149 (2017) 56–80.  
 [7] M. Benes, J. Tichy, On coupled Navier-Stokes and energy equations in exterior-like domains, *Comput. Math. Appl.* 70 (2015) 2867–2882.  
 [8] C. Bertoglio, A. Caiazzo, A tangential regularization method for backflow stabilization in hemodynamics, *J. Comput. Phys.* 261 (2014) 162–171.  
 [9] E. Bilgen, H. Oztop, Natural convection heat transfer in partially open inclined square cavities, *Int. J. Heat Mass Transf.* 48 (2005) 1470–1479.  
 [10] M. Braack, P. Mucha, Directional do-nothing condition for the navier-stokes equations, *J. Comput. Math.* 32 (2014) 507–521.  
 [11] C.-H. Bruneau, P. Fabrie, Effective downstream boundary conditions for incompressible Navier-Stokes equations, *Int. J. Numer. Methods Fluids* 19 (1994) 693–705.  
 [12] C.-H. Bruneau, P. Fabrie, New efficient boundary conditions for incompressible navier-stokes equations: a well-posedness result, *Math. Model. Numer. Anal.* 30 (1996) 815–840.  
 [13] A. Ceretani, C. Rautenberg, The boussinesq system with mixed non-smooth boundary conditions and do-nothing boundary flow, *Z. Angew. Math. Phys.* 70 (2019) 14.  
 [14] Y. Chan, C. Tien, A numerical study of two-dimensional laminar natural convection in shallow open cavities, *Int. J. Heat Mass Transf.* 28 (1985) 603–612.  
 [15] Y. Chan, C. Tien, A numerical study of two-dimensional natural convection in square open cavities, *Numer. Heat Transf.* 8 (1985) 65–80.  
 [16] Y. Chan, C. Tien, Laminar natural convection in shallow open cavities, *J. Heat Transf.* 108 (1986) 305–309.  
 [17] V. Chiriac, A. Ortega, A numerical study of the unsteady flow and heat transfer in a transitional confined slot jet impinging on an isothermal surface, *Int. J. Heat Mass Transf.* 45 (2002) 1237–1248.  
 [18] S. Chung, K. Vafai, Vibration induced mixed convection in an open-ended obstructed cavity, *Int. J. Heat Mass Transf.* 53 (2010) 2703–2714.  
 [19] G. Comini, C. Nonino, The outflow boundary condition for mixed convection problems, *Trans. Eng. Sci.* 18 (1998) 83–92.  
 [20] J. Davalath, Y. Bayazitoglu, Forced convection cooling across rectangular blocks, *J. Heat Transf.* 109 (1987) 321–328.  
 [21] G. Desrayaud, E. Chenier, A.J. et al, Benchmark solutions for natural convection flows in vertical channels submitted to different open boundary conditions, *Int. J. Thermal Sci.* 72 (2013) 18–33.  
 [22] S. Dong, An outflow boundary condition and algorithm for incompressible two-phase flows with phase field approach, *J. Comput. Phys.* 266 (2014) 47–73.  
 [23] S. Dong, A convective-like energy-stable open boundary condition for simulations of incompressible flows, *J. Comput. Phys.* 302 (2015) 300–328.  
 [24] S. Dong, G. Karniadakis, DNS of flow past stationary and oscillating cylinder at  $Re = 10,000$ , *J. Fluids Struct.* 20 (2005) 14–23.  
 [25] S. Dong, G. Karniadakis, C. Chrysostomidis, A robust and accurate outflow boundary condition for incompressible flow simulations on severely-truncated unbounded domains, *J. Comput. Phys.* 261 (2014) 83–105.  
 [26] S. Dong, G. Karniadakis, A. Ekmekci, D. Rockwell, A combined direct numerical simulation-particle image velocimetry study of the turbulent near wake, *J. Fluid Mech.* 569 (2006) 185–207.  
 [27] S. Dong, J. Shen, A pressure correction scheme for generalized form of energy-stable open boundary conditions for incompressible flows, *J. Comput. Phys.* 291 (2015) 254–278.  
 [28] S. Dong, X. Wang, A rotational pressure-correction scheme for incompressible two-phase flows with open boundaries, *PLOS One* 11(5) (2016) e0154565.  
 [29] M. Engelman, M.-A. Jamnia, Transient flow past a circular cylinder: A benchmark solution, *Int. J. Numer. Methods Fluids* 11 (1990) 985–1000.  
 [30] M. Feistauer, T. Neustupa, On the existence of a weak solution of viscous incompressible flow past a cascade of profiles with an arbitrarily large inflow, *J. Math. Fluid Mech.* 15 (2013) 701–715.  
 [31] E. Fontana, A. Silva, V. Mariani, Natural convection in a partially open square cavity with internal heat source: an analysis of the opening mass flow, *Int. J. Heat Mass Transf.* 54 (2011) 1369–1386.  
 [32] M. Forestier, R. Pasquetti, R. Peuret, C. Sabbah, Spatial development of wakes using a spectral multi-domain method, *Appl. Numer. Math.* 33 (2000) 207–216.  
 [33] J. Fouchet-Incaux, Artificial boundaries and formulations for the incompressible navier-stokes equations. applications to air and blood flows, *SeMA J.* 64 (2014) 1–40.  
 [34] G. Gan, Impact of computational domain on the prediction of buoyance-driven ventilation cooling, *Build. Environ.* 45 (2010) 1173–1183.  
 [35] D. Gartling, A test problem for outflow boundary conditions – flow over a backward-facing step, *Int. J. Numer. Methods Fluids* 11 (1990) 953–967.  
 [36] V. Gravemeier, A. Comerford, L. Yoshihara, M. Ismail, W. Wall, A novel formulation for Neumann inflow boundary conditions in biomechanics, *Int. J. Numer. Methods Biomed. Eng.* 28 (2012) 560–573.

- [37] P. Gresho, Incompressible fluid dynamics: some fundamental formulation issues, *Annu. Rev. Fluid Mech.* 23 (1991) 413–453.
- [38] J. Guermond, P. Mineev, J. Shen, Error analysis of pressure-correction schemes for the time-dependent Stokes equations with open boundary conditions, *SIAM J. Numer. Anal.* 43 (2005) 239–258.
- [39] M. Ismail, V. Gravemeier, A. Comerford, W. Wall, A stable approach for coupling multidimensional cardiovascular and pulmonary networks based on a novel pressure-flow rate or pressure-only Neumann boundary condition formulation, *Int. J. Numer. Methods Biomed. Eng.* 30 (2014) 447–469.
- [40] G. Karniadakis, S. Sherwin, *Spectral/hp element methods for computational fluid dynamics*, 2nd edn., Oxford University Press, 2005.
- [41] J. Keskar, D. Lyn, Computations of a laminar backward-facing step flow at  $Re=800$  with a spectral domain decomposition method, *Int. J. Numer. Methods Fluids* 29 (1999) 411–427.
- [42] C. Kettleborough, Transient laminar free convection between heated vertical plates including entrance effects, *Int. J. Heat Mass Transf.* 15 (1972) 883–896.
- [43] K. Khanafar, K. Vafai, Effective boundary conditions for buoyance-driven flows and heat transfer in fully open-ended two-dimensional enclosures, *Int. J. Heat Mass Transf.* 45 (2002) 2527–2538.
- [44] S. Lal, C. Reji, Numerical prediction of natural convection in vented cavities using restricted domain approach, *Int. J. Heat Mass Transf.* 52 (2009) 724–734.
- [45] M. Lanzendorfer, J. Stebel, On pressure boundary conditions for steady flows of incompressible fluids with pressure and shear rate dependent viscosities, *Appl. Math.* 56 (2011) 265–285.
- [46] H. Lee, M. Ha, H. Yoon, A numerical study on the fluid flow and heat transfer in the confined jet flow in the presence of magnetic field, *Int. J. Heat Mass Transf.* 48 (2005) 5297–5309.
- [47] H. Lee, H. Yoon, M. Ha, A numerical investigation on the fluid flow and heat transfer in the confined impinging slot jet in the low Reynolds number region for different channel heights, *Int. J. Heat Mass Transf.* 51 (2008) 4055–4068.
- [48] J. Leone, Open boundary condition symposium benchmark solution: stratified flow over a backward-facing step, *Int. J. Numer. Methods Fluids* 11 (1990) 969–984.
- [49] P.-W. Li, W.-Q. Tao, Effects of outflow boundary condition on convective heat transfer with strong recirculating flow, *Wärme-und Stoffübertragung* 29 (1994) 463–470.
- [50] M. Moghadam, Y. Bazilevs, T.-Y. Hsia, I. Vignon-Clementel, A. Marsden, A comparison of outlet boundary treatments for prevention of backflow divergence with relevance to blood flow simulations, *Comput. Mech.* 48 (2011) 277–291.
- [51] T. Neustupa, The weak solvability of the steady problem modelling the flow of a viscous incompressible heat-conductive fluid through the profile cascade, *Int. J. Numer. Methods Heat Fluid Flow* 27 (2017) 1451–1466.
- [52] N. Ni, Z. Yang, S. Dong, Energy-stable boundary conditions based on a quadratic form: Applications to outflow/open-boundary problems in incompressible flows, *J. Comput. Phys.* 391 (2019) 179–215.
- [53] M. Olshanskii, V. Staroverov, On simulation of outflow boundary conditions in finite difference calculations for incompressible fluid, *Int. J. Numer. Methods Fluids* 33 (2000) 499–534.
- [54] I. Orlanski, A simple boundary condition for unbounded hyperbolic flows, *J. Comput. Phys.* 21 (1976) 251–269.
- [55] C. Perez, J.-M. Thomas, S. Blancher, R. Creff, The steady Navier-Stokes/energy system with temperature-dependent viscosity – part 1: Analysis of the continuous problem, *Int. J. Numer. Methods Fluids* 56 (2008) 63–89.
- [56] C. Perez, J.-M. Thomas, S. Blancher, R. Creff, The steady Navier-Stokes/energy system with temperature-dependent viscosity – part 2: The discrete problem and numerical experiments, *Int. J. Numer. Methods Fluids* 56 (2008) 91–114.
- [57] A. Porpora, P. Zunino, C. Vergara, M. Piccinelli, Numerical treatment of boundary conditions to replace branches in hemodynamics, *Int. J. Numer. Methods Biomed. Eng.* 28 (2012) 1165–1183.
- [58] M. Ruith, P. Chen, E. Meiburg, Development of boundary conditions for direct numerical simulations of three-dimensional vortex breakdown phenomena in semi-infinite domains, *Comput. Fluids* 33 (2004) 1225–1250.
- [59] R. Sani, P. Gresho, Resume and remarks on the open boundary condition minisymposium, *Int. J. Numer. Methods Fluids* 18 (1994) 983–1008.
- [60] S. Sherwin, G. Karniadakis, A triangular spectral element method: applications to the incompressible Navier-Stokes equations, *Comput. Meth. Appl. Mech. Eng.* 123 (1995) 189–229.
- [61] K. Shirvan, M. Mamourian, S. Mirzakhani, R. Ellahi, K. Vafai, Numerical investigation and sensitivity analysis of effective parameters on combined heat transfer performance in a porous solar cavity receiver by response surface methodology, *Int. J. Heat Mass Transf.* 105 (2017) 811–825.
- [62] A. Sommerfeld, *Partial Differential Equations in Physics*, Academic Press, 1949.
- [63] S. Taylor, J. Rance, J. Medwell, A note on the imposition of traction boundary conditions when using the FEM for solving incompressible flow problems, *Commun. Appl. Numer. Methods* 1 (1985) 113–121.
- [64] K. Vafai, J. Eftefagh, The effects of sharper corners on buoyance-driven flows with particular emphasis on outer boundaries, *Int. J. Heat Mass Transf.* 33 (1990) 2311–2328.
- [65] S. Varghese, S. Frankel, P. Fischer, Direct numerical simulation of stenotic flows. Part 1. Steady flow, *J. Fluid Mech.* 582 (2007) 253–280.
- [66] Z. Yang, S. Dong, Multiphase flows of  $N$  immiscible incompressible fluids: an outflow/open boundary condition and algorithm, *J. Comput. Phys.* 366 (2018) 33–70.
- [67] T. Young, K. Vafai, Convective flow and heat transfer in a channel containing multiple heated obstacles, *Int. J. Heat Mass Transf.* 41 (1998) 3279–3298.
- [68] J.-H. Zhang, D.-D. Zhang, D. Liu, F.-Y. Zhao, Y. Li, H.-Q. Wang, Free vent boundary conditions for thermal buoyance driven laminar flows inside open building enclosures, *Build. Environ.* 111 (2017) 10–23.
- [69] X. Zheng, S. Dong, An eigen-based high-order expansion basis for structured spectral elements, *J. Comput. Phys.* 230 (2011) 8573–8602.